

Contents lists available at ScienceDirect

Materials Today Physics

journal homepage: www.journals.elsevier.com/materials-today-physics





Phonon ray tracing calculations of ballistic temperature and heat flux profiles in nanostructures

Yingru Song, Geoff Wehmeyer

Mechanical Engineering, William Marsh Rice University, Houston, TX, 77005, USA

ARTICLE INFO

Keywords:
Ray tracing
Ballistic phonon transport
Nanoporous materials
Thermal transport
Landauer theory

ABSTRACT

Phonon ray tracing calculations have been used to quantify phonon boundary scattering in nanomaterials and to interpret thermal conductivity measurements. However, Landauer-based phonon ray tracing methods have not been able to access the temperature or heat flux profiles within nanomaterials, meaning that computationally intensive Boltzmann Transport Equation solvers are needed to gain insight into ballistic transport physics or model nanoscale temperature mapping experiments. Here, we derive and apply phonon Monte Carlo ray tracing methods to calculate the local temperature and local heat flux in semiconducting nanomaterials, with a focus on the ballistic transport regime. The derivation provides a straightforward interpretation of the local temperature in terms of a thermal conductance ratio, and the local heat flux in terms of the difference between forward- and reverse-oriented phonon trajectories crossing a control surface. After validating the method for several common transport regimes and geometries, we apply the method to optimize geometric parameters that lead to locally inverted temperature gradients in porous nanomeshes, and to evaluate the heat focusing capabilities of geometric ballistic phonon lenses. These applications illustrate how phonon ray tracing methods can be used to quantify ballistic thermal profiles and to design nanostructures that exhibit atypical thermal behaviors in the ballistic regime.

1. Introduction

The development of micro/nanoscale thermal metrologies and nanofabrication capabilities has enabled researchers to explore geometry-dependent heat conduction in semiconducting nanomaterials [1–3]. When the characteristic lengthscale ($L_{\rm char}$) of the nanomaterial is large compared to the phonon mean free path (Λ), continuum finite-element methods or solutions to the macroscopic heat equation using Fourier's law are used to quantify the geometry-dependent heat flux (q) and temperature (T) fields. These continuum methods fail to capture the size-dependent thermal properties that arise due to phonon interactions with the boundaries of the system (classical size effect) or phonon dispersion modifications (quantum size effect) [4]. For systems with single-digit nanometer $L_{\rm char}$, atomistic techniques including molecular dynamics [5] or atomistic Green's function [6] methods are successfully used to find the geometry-dependent q and T, although computational constraints limit the number of atoms that can be considered.

Experiments probing nanostructures with $L_{\rm char}$ ranging from tens to

hundreds of nanometers typically analyze results using numerical or analytical solutions of the phonon Boltzmann Transport Equation (BTE) [7,8]. The BTE is applicable in the mesoscopic regime when L_{char} is large compared to the dominant phonon wavelengths (λ), and accurately quantifies geometry-dependent heat conduction in both the ballistic $(L_{\text{char}} \ll \Lambda)$ and diffusive $(L_{\text{char}} \gg \Lambda)$ regimes. A typical steady-state BTE approach solves a high-dimensional integrodifferential equation to find the phonon modewise distribution function (f), and then uses f to calculate q and T in the device [9–14]. Researchers have developed computational methods based on variance-reduced Monte Carlo approaches to perform these BTE calculations for realistic three-dimensional experimental geometries [15-17], and have developed single-phonon trajectory tracking schemes to determine the local T profile and total heat transfer [18,19]. Even after making simplifying approximations such as the relaxation time approximation (RTA), BTE solutions are challenging because the distribution function depends on the time t, three real-space coordinates x, y, z, three components of the phonon wavevector k_x, k_y, k_z , and the phonon polarization index s.

As an alternate approach to the BTE, thermal researchers have also

E-mail address: gpw1@rice.edu (G. Wehmeyer).

 $^{^{\}ast}$ Corresponding author.

developed phonon ray tracing methodologies [20-29] to study heat transfer in mesoscopic devices. These phonon ray tracing methods track phonon trajectories through the device and use the trajectory information to determine the phonon mean free path in the nanostructure via a Landauer approach [20]. The ray tracing techniques are efficient in the ballistic regime because all phonon trajectories can be calculated in parallel, energy conservation is explicitly enforced without the need for iteration or integration over modes, explicit time-stepping and meshing issues can be avoided via direct trajectory calculation, and convergence can be established statistically via Monte Carlo methods [22]. It is typical to assume in the ray tracing that the material has an isotropic phonon dispersion relation, though anisotropy can be included at additional computational cost [21]. Rigorous descriptions of inelastic phonon-phonon scattering are difficult to incorporate within ray tracing, making the results from ray tracing calculations functionally equivalent to BTE solutions under the RTA.

One major current advantage of the BTE compared to ray tracing is that the local q and T profiles can be readily obtained from the BTE solution and used to assist in the interpretation of geometry dependent thermal transport. For example, the *q* and *T* outputs from BTE solutions have been used to study ballistic transport phenomena in nanoporous materials [12], locally inverted temperature gradients in nanocomposites [30,31], and heat focusing via ballistic phonon geometric lensing [32]. In addition to the interest in interpreting transport phenomena, recent developments in nanothermometry techniques using scanning probes [33], luminescent nanoparticles [34], or electron microscopy signals [35,36] may open new opportunities for direct nanoscale measurements of temperature profiles and comparison against mesoscopic simulation. Unfortunately, existing Landauer ray tracing methods are not able to predict these T and q profiles inside devices, which makes it difficult to explore ballistic phonon transport in nanomaterials or validate nanothermal experiments.

Here, we describe and apply numerical methods to extract the local T and q profiles in nanomaterials using phonon ray tracing simulations. The T profile is found as a ratio of local reservoir-to-probe thermal conductances obtained via a Landauer-Büttiker method, and the q profile is calculated by tracking the phonon trajectories across a control surface. Our validation studies for fully dense structures and nanowire geometries show that method accurately calculates the T and q profiles from the ballistic through diffusive regimes, though the method is most computationally efficient in the ballistic regime. After establishing the method, we then apply the ray tracing methods to establish the optimal geometric parameters to observe locally inverted temperature gradients in nanoporous materials [30,31]. Here, the phrase "locally inverted" means that the polarity of the local *T* gradient in the ballistic regime is inverted as compared to the familiar Fourier law diffusive prediction. We also use the ray tracing simulations to study geometric ballistic phonon focusing [32] in nanoporous materials; in these devices, the local T and local q profiles can be spatially localized at the focal point of a set of radially aligned pores. These demonstrations show that the phonon ray tracing method can be used to design structures with unique and optimized ballistic thermal phonon behaviors.

2. Methods and derivation

The derivations consider a thermal device of interest connected to two thermalizing reservoirs, as shown in Fig. 1. The hot reservoir is at a temperature T_h and has a contact area A_h with the device, while the cold reservoir is at a temperature T_c with a contact area A_c . Within a Landauer-like picture of transport, phonons are injected into the device from both reservoirs. Throughout our derivations, we assume that the reservoirs are thermally isotropic and homogeneous materials; the device itself can be heterogeneous, as illustrated by the pores in Fig. 1.

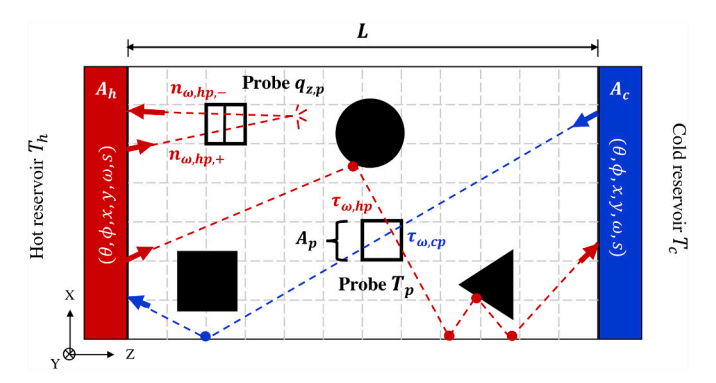


Fig. 1. Ray tracing illustration. Schematic of phonon ray tracing trajectories used to determine the local temperature and heat flux profiles. Phonons with initial location (x,y), initial propagation direction (θ,φ) , frequency ω , and polarization index s are initialized at the hot (red) and cold (blue) thermalizing reservoirs with device-reservoir contact areas A_h and A_c , respectively. The phonon trajectories are traced through the device until the phonon reaches either thermalizing reservoir. The Landauer model considers a probe with location index p. The phonon hot-probe and cold-probe transmission coefficients τ_{hp} and τ_{cp} , respectively, are used to determine the local probe temperature T_p . The phonon forward-crossing index $n_{hp,+}$ and reverse-crossing index $n_{hp,+}$ are used to calculate the local z-component of the probe heat flux, $q_{z,p}$.

2.1. Local heat flux derivation

We begin by deriving an expression for the steady-state heat flux inside the device. We focus here on the z-component of the heat flux q_z , as it is straightforward to modify the approach to find the other two components q_x and q_y . We consider a control surface (also referred to as a "probe" in reference to the T derivation discussed below) with area A_p and a surface normal oriented in +z.

Consider a phonon labeled by the index j. This index is shorthand for the phonon initial location (x, y) at the reservoir-device contact, the initial polar and azimuthal propagation angle (θ, φ) upon entering the device from the reservoir, the phonon frequency ω , and the polarization index s. This phonon is assumed to undergo elastic (i.e., frequencypreserving) interactions within the device before exiting the device after a residence time t_i ; the method does not consider any phonon absorption/emission within the device. During this time in the device, this phonon passes across the control surface area A_p a total of $n_{j,p,+}$ times in the +z direction and $n_{j,p,-}$ times in the -z direction; both of these integers are larger than unity in general. For example, phonons may undergo multiple backscattering events due to the interactions with other phonons or diffuse surfaces of pores [9,37,38], which results in phonon trajectories with velocity components in the -z direction, although the initial velocity component projection is in the +z direction. The net energy transfer across the probe by this phonon during its transit through the device is $\hbar\omega(n_{j,p,+}-n_{j,p,-})$. The time-averaged *z*-component of the heat flux at the probe due to the j^{th} phonon $q_{z,p,j}$ is therefore

$$q_{z,p,j} = \frac{\hbar\omega(n_{j,+} - n_{j,-})}{A_p t_j}.$$
 (1)

Here, the heat flux contributed by this phonon is interpreted as the net energy transfer divided by the residence time t_j of this phonon and by the probe surface area. t_j is the time spent in the domain by the phonon before it exits at a reservoir. As discussed below, t_j appears as an intermediate variable in the derivation and does not need to be determined to find the heat flux.

During this phonon residence time t_j , the number of similar phonons injected into the device from the reservoir within a differential reservoir area dA, differential solid angle $d\Omega \equiv \sin\theta d\theta d\phi$, and differential angular frequency $d\omega$ of phonon j described above is

$$N_{j} = f_{0}(T_{\text{res}}) \frac{D(\omega)}{4\pi} t_{j} v \cos \theta d\Omega d\omega dA, \tag{2}$$

where $f_0(T_{\rm res})=1/\left(\exp\left(\frac{\hbar\omega}{k_BT_{\rm res}}\right)-1\right)$ is the Bose-Einstein distribution at the reservoir temperature $T_{\rm res}$, $D(\omega)$ is the density of states per unit volume of the reservoir material, $v\cos\theta$ is the z component of the phonon velocity in the reservoir, $k_{\rm B}$ is Boltzmann's constant, and \hbar is Planck's reduced constant. For the isotropic reservoir materials considered here, v depends on ω and s but is independent of θ . Conceptually, the residence time t_j appears in Eq. (2) to accurately account for the total number of phonons injected into the device, as the injection occurs at a fixed rate given by N_i/t_i .

The differential contribution towards the average probe heat flux $dq_{zp}=N_jq_{zp,j}$ is therefore obtained using Eqs. (1) and (2) as

$$dq_{z,p} = N_j q_{z,p,j} = \frac{\hbar \omega \left(n_{j,p,+} - n_{j,p,-} \right)}{A_p} f_0(T_{\text{res}}) \frac{D(\omega)}{4\pi} v \cos \theta d\Omega d\omega dA. \tag{3}$$

Note that the phonon residence time t_j does not appear in Eq. (3), meaning that this quantity does not need to be recorded in order to calculate the heat flux. Considering all initial locations and initial angles of both reservoirs, the *z*-component of the heat flow at the probe is obtained as

$$q_{z,p} = \sum_{s} \int_{\omega} \int_{\Omega=0}^{2\pi} \int_{A_{h}} \frac{\hbar \omega (n_{j,hp,+}, -n_{j,hp,-})}{A_{p}} f_{0}(T_{h}) \frac{D(\omega)}{4\pi} v \cos \theta dA_{h} d\Omega d\omega$$

$$+ \sum_{s} \int_{\omega} \int_{\Omega=0}^{4\pi} \int_{A_{p}} \frac{\hbar \omega (n_{j,cp,+} - n_{j,cp,-})}{A_{p}} f_{0}(T_{c}) \frac{D(\omega)}{4\pi} v \cos \theta dA_{c} d\Omega d\omega.$$
(4)

Thoughout this work the sum is taken over all polarizations s, and the integrals over ω are taken over all phonon frequencies supported by the respective reservoirs. The subscripts hp and cp in Eq. (4) indicate that the phonon trajectories are initiated at the hot and cold reservoirs, respectively.

Eq. (4) can be simplified further using considerations of detailed balance. If $T_h = T_c$, the second law of thermodynamics requires that the heat flux vanishes, meaning that the two terms on the right hand side of Eq. (4) must cancel for $T_h = T_c$. In the linear response regime in which the only temperature dependence arises due to the T-dependent occupation statistics, we insert a Taylor series expansion of the Bose-Einstein statistics as $f_0(T_h) = f_0(T_c) + \frac{\partial f_0}{\partial T}(T_h - T_c)$ into Eq. (4), use the detailed balance requirement, and obtain

$$q_{z,p} = (T_h - T_c) \sum_{s} \int_{\omega} \int_{\Omega=0}^{2\pi} \int_{A_h} \frac{\hbar \omega \left(n_{j,hp,+} - n_{j,hp,-} \right)}{A_p} \frac{\partial f_0}{\partial T} \frac{D(\omega)}{4\pi} v \cos \theta dA_h d\Omega d\omega.$$
(5)

Lastly, introducing the modewise heat capacity $C_{\omega} \equiv \hbar \omega D(\omega) \frac{\partial f_0}{\partial T}$ used to calculate the total volumetric heat capacity $C \equiv \sum_{s} \int_{\omega} C_{\omega} d\omega$, this final expression for the local *z*-component of the heat flux can be written as

$$q_{z,p} = \frac{(T_h - T_c)}{4\pi A_p} \sum_{s} \int_{\Omega} \int_{\Omega_c}^{2\pi} \int_{\Omega_c} \left(n_{j,hp,+} - n_{j,hp,-} \right) C_{\omega} v \cos\theta dA_h d\Omega d\omega.$$
 (6)

Eq. (6) shows a general expression for the heat flux, which is obtained by integrating over each phonon frequency, initial location, and initial angular distribution. The position dependence of the heat flux within the device is captured entirely by the difference between forward- and reverse-oriented crossings $(n_{j,hp,+} - n_{j,hp,-})$, which in general depends on the probe location index p. Below we present our results in non-dimensional terms using the dimensionless z-component of the heat flux

$$Q_p \equiv \frac{q_{z,p}}{\frac{1}{2}\overline{Cv}(T_h - T_c)},\tag{7}$$

where $\overline{Cv} \equiv \sum\limits_{s} \int C_{\omega} v d\omega$ is the frequency-averaged product of the modewise specific heat and modewise group velocity. The non-dimensionalization is selected such that $Q_p=1$ in the case of fully ballistic heat transfer between hot and cold reservoirs, as verified in Section 3.1 below.

2.2. Local temperature derivation

To find the local temperature, we leverage the multi-terminal Landauer-Büttiker theory describing phonon transport in nanomaterials [22,29,39–41]. Here, we use the term "terminal" to refer both to the thermalizing hot and cold reservoirs and to a thermal probe located inside the device. Within the Landauer-Büttiker theory [22], the two-terminal thermal conductance between terminal a and b is

$$G_{ab} = \frac{A_a}{4} \sum_{s} \int_{\omega} C_{\omega} v \, \overline{\tau_{\omega,ab}} d\omega, \tag{8}$$

where A_a is the contact area of terminal a and the weighted modewise area- and angle-averaged phonon transmissivity from a to b is

$$\overline{\tau_{\omega,ab}} = \frac{1}{A_a \pi} \int_{\Omega} \int_{A_a} \tau_{\omega,ab} \cos \theta dA_a d\Omega. \tag{9}$$

Here, $\tau_{\omega,ab}$ is the phonon transmissivity from a to b for a given choice of ω,s,Ω , and initial location on terminal a. The normalization prefactor $(A_a\pi)^{-1}$ in Eq. (9) is selected such that $\overline{\tau_{\omega,ab}}=1$ if $\tau_{\omega,ab}=1$ for all phonons. The integral over solid angles spans all Ω oriented such that phonons are exiting reservoir a and propagating in the device (e.g., Ω would range from 0 to 2π steradians for the hot reservoir shown in Fig. 1 (a)). In a linear system that obeys time-reversal symmetry, the thermal conductance from a to b (G_{ab}) and the thermal conductance from b to a (G_{ba}) are identical. $\overline{\tau_{\omega,ab}}$ is a primary output of the phonon ray tracing, and is interpreted as the weighted probability of phonon energy transmission between terminals a and b.

Here we consider a thermalizing blackbody probe inserted at an arbitrary location inside the system indexed by p, and consider the device as a three-terminal system with a thermalizing hot reservoir, cold reservoir, and probe. Phonons from each of the reservoirs can be transmitted to and absorbed by the probe; similarly, the probe emits as a blackbody at a temperature T_p , which is the local temperature of interest. According to multi-terminal Landauer-Büttiker theory [4,42], the net heat flow from reservoirs to the probe is

$$Q_{p} = G_{hp}(T_{h} - T_{p}) + G_{cp}(T_{c} - T_{p}), \tag{10}$$

where G_{hp} and G_{cp} are the thermal conductance from the hot and cold reservoir to the probe, respectively, calculated using Eqs. (8) and (9). Local thermal equilibrium is set by dictating $Q_p=0$; physically, this represents the case where a fully thermalizing, adiabatic probe is inserted into the device. Solving for the dimensionless temperature $\theta_p\equiv \frac{T_p-T_c}{T_h-T_c}$ by setting $Q_p=0$ in Eq. (10), we obtain the final expression for the dimensionless temperature as

$$\theta_p = \frac{G_{hp}}{G_{t-} + G}.\tag{11}$$

This result is exactly analogous to the corresponding Landauer-Büttiker expression for the voltage measured at a probe in a mesoscopic electrical transport experiment [43], as expected. Eq. (11) shows that the expression for the local dimensionless temperature can be obtained by calculating the thermal conductance from both reservoirs to the probe. Because both G_{hp} and G_{cp} always must be larger than unity to satisfy the second law of thermodynamics, the right hand side in Eq. (11) is bounded between zero and unity, indicating that the temperature T_p is bounded between the temperatures of the hot and cold reservoirs at all locations in the device.

Physically, the temperature calculated in Eq. (11) represents the equilibrium temperature that would be reached by a thermalizing probe. This maximally intrusive probe temperature is well defined from the ballistic through diffusive regime, and we show below that the spatial dependence of the T profile agrees with the T profiles obtained from solutions of the BTE under the RTA for several traditional geometries. In BTE simulations, the T rise is typically extracted using the instantaneous internal phonon energy within a mesh volume and the local specific heat [9]; in contrast, the internal energy is not explicitly calculated in the ray tracing. We also note that in experiments, the probe used to measure T may not behave as a blackbody phonon absorber and emitter (i.e., not all phonons that are incident on the probe may be absorbed/re-emitted). The ray tracing methodology could be extended to model these experiments by selecting non-blackbody phonon transmission at the probes, though this approach is not considered further here.

We now compare our methodology against existing BTE solution procedures [7]. The traditional BTE numerical approach aims to solve for the phonon modewise distribution function f as a function of position and time; once f is known, it is straightforward to find the local temperature profiles and heat flux profiles [9-13]. In many cases, f is found by injecting many phonons (or bundles of phonons) into a domain, tracking the positions on a mesh as a function of time as phonon drift and scatter, and recording the phonon statistics at each mesh location and time [7]. Some of these BTE methods use Monte Carlo approaches to determine aspects of the phonon trajectory evolution or to model the phonon scattering events [9,12,13,15,16,18,19]. Typically, simulations are performed as a function of time and the locations of all phonons (or bundles representing groups of phonons) must be considered simultaneously; however, researchers have also developed BTE numerical solutions that use a series of single-phonon trajectory calculations to determine the steady-state local energy and temperature within a meshed cell [18,19].

In contrast, the ray tracing model described here fundamentally determine the phonon transmission coefficients and forward/reverse crossing indices rather than determining the local energy density or local heat flux as a function of time in a volumetric mesh. The advantage of this ray tracing method is that ballistic results are obtained in a computationally efficient manner, and the phonon trajectory calculations are easily parallelizable. The theoretical framework is steady-state. meaning that a timestep/final simulation time convergence is not explicitly required; rather, convergence is established by increasing the total number of simulated trajectories. The calculation of the global heat flow in the previous single-phonon BTE calculation [18,19] has several conceptual similarities to the ray tracing implementation described here, though the current ray tracing formalism is also able to access the local heat flux in addition to the global heat flow. The disadvantages of the Landauer approach are that phonon-phonon scattering is not rigorously incorporated, and that transient temperature or heat flux fields are not accessible.

2.3. Ray tracing implementation

We calculated the temperature and heat flux using a ray tracing technique implemented in MATLAB [20,22,23]. The geometry and coordinate system is defined in Fig. 1, and considers a hot reservoir at z=0 and a cold reservoir at z=L, where L is the device length. To calculate T and q, we apply a volumetric mesh to the device and consider each mesh element as a probe. An advantage of the ray tracing method is that the mesh selection can enforce the required symmetry of the T and q profiles. We perform mesh convergence studies in all cases to ensure mesh-independent results; intentionally large probe volumes could be used to simulate experiments with non-vanishing probe size, though we

do not consider these large probes further in this work. The computational disadvantage in using smaller mesh sizes is that more phonon trajectories need to be implemented to reduce the statistical error at the probe associated with the Monte Carlo method, as discussed further in Section 2.5 below. We now describe the implementation of the T and q mapping before discussing simplified results for the case of fully ballistic transport.

2.3.1. Local temperature mapping implementation

Eqs. (8) and (11) show that the local probe temperature T_p is determined by the thermal conductance G_{ab} and more explicitly, the average transmissivity $\overline{\tau_{ab}}$. We calculate $\overline{\tau_{hp}}$ and $\overline{\tau_{cp}}$ by a set of phonon trajectory calculations. In each trajectory calculation, a single phonon is emitted from a thermal reservoir at z = 0 or z = L in Fig. 1. To initialize the phonons at the reservoir, we use four random numbers selected from a uniform distribution bounded by 0-1 to determine the initial location and direction. The initial location (x, y) is uniformly selected within the cross-sectional area of the reservoir A_h or A_c . The initial propagation direction is determined by the azimuthal angle (φ) , which is uniformly distributed from 0 to 2π , and the polar angle (θ) which is selected by $\theta =$ $\sin^{-1}\sqrt{R_1}$ where R_1 is a random number selected from a uniform distribution bounded by 0 and 1. This initial direction (φ, θ) obeys the isotropic solid angle weighted distribution that is familiar from photon black-body radiation [44]. The final area- and angle-averaged transmissivity $\overline{\tau_{ab}}$ is calculated by implementing a large number of these phonon trajectories with different initial conditions. We estimate the statistical error in the transmission coefficients using a previously described sub-sampling method [22].

We track the phonon trajectory through the device until the phonon transmits to the far reservoir or is backscattered to the initial reservoir. In the fully ballistic case, the phonon travels until it encounters a boundary. In the scenario where bulk-like elastic volumetric scattering inside the material is considered, we dictate this bulk mean free path Λ as an input parameter to the calculation. After a phonon scattering event (ether boundary or volumetric), we select a bulk free path from a logarithmically weighted distribution as $- \Lambda \ln(R_2)$, where R_2 is a random number selected from 0 to 1. The free path selection $-\Lambda \ln(R_2)$ represents a distribution in which the probability of scattering after travelling a distance l is found to be $1 - \exp(-l/\Lambda)$. The term $-\ln(R_2)$ ensures that the probability of scattering follows the typical weighed exponential distribution of free paths [45]. If the volumetric free path is smaller than the distance to the next surface on the phonon's trajectory, the phonon is propagated to the location of volumetric scattering and the outgoing direction after the scattering is uniformly weighted within the 4π steradian solid angle. If the volumetric free path is larger than the distance to next surface collision, the phonon is propagated to the scattering surface and the outgoing phonon direction can be selected as diffuse or specular. Here, we consider diffuse scattering unless otherwise noted, which is appropriate when the boundaries have characteristic surface roughness/disorder at scales comparable to or larger than the phonon wavelengths [4].

The thermalizing probe is not explicitly included in the trajectory calculations and is only considered after the trajectory has terminated at a reservoir. During the phonon's transit in the device, we record a binary variable indicating whether a phonon trajectory has intersected the mesh volume representing a potential probe location. If the thermalizing probe were present at that location, the phonon would have been absorbed, and we record the reservoir-probe transmission as unity for that trajectory and probe location. The advantage in this method is a single set of phonon trajectories can be used for all probe locations, dramatically improving the computational efficiency. For sufficiently small mesh sizes, the temperature value calculated using the method approaches the intrinsic (i.e., mesh-independent) $T_{\rm p}$ limit reflecting the thermalization temperature of an infinitesimally small blackbody probe interacting only with the reservoirs and no other probes. The

temperature calculation in Eq. (8) requires only the reservoir-to-probe transmissivities to be calculated, meaning that the probe-to-reservoir transmission due to phonons emitted from the probe is not required and that phonon re-emission from the probe is not implemented.

2.3.2. Local heat flux implementation

Consider a number N_ω of phonon trajectories for phonons with the frequency range between ω and $\omega+d\omega$ near ω . The integrals over position and angle in Eq. (6) are statistically approximated by selecting random numbers from a weighted distribution to initialize the phonon trajectories; this angular and position weighting to find q is identical to the T calculation described in Section 2.3.1 above. After initializing the phonon trajectories and tracing these phonons through the device, the output from the calculation is the number of phonon trajectories passing through the probe surface in the positive (negative) z direction $N_{\omega,hp,+}(N_{\omega,hp,-})$, which is determined by calculating the z-component velocity of the phonon when its trajectory intersects the control surface. Each phonon trajectory can pass through the same probe multiple times in the algorithm. The numerical approximation to Eq. (6) therefore becomes

$$q_{z,p} = \frac{(T_h - T_c)}{4} \frac{A_h}{A_p} \sum_{s} \int_{\omega} C_{\omega} v \frac{(N_{\omega,hp,+} - N_{\omega,hp,-})}{N_{\omega}} d\omega.$$
 (12)

Note that q_{zp} denotes the total net heat flux in the z direction passing through the probe; even though the phonons are only initialized from the hot reservoir in the ray tracing calculations, the theory described here accurately describes the interactions between both hot and cold reservoirs.

2.4. Limiting case: Ballistic transport

The ray tracing is most computationally efficient in the ballistic regime in which T and q are determined by boundary scattering. If all of the phonons interact with each bounding surface similarly (e.g., in a diffuse or specular manner), the transmissivities and the phonon surface crossing outputs from the ray tracing are independent of ω and s. As a result, the dimensionless temperature expression in Eq. (11) simplifies to

$$\theta_p = \frac{\overline{\tau_{hp}}}{\overline{\tau_{hp}} + \overline{\tau_{cp}}}.\tag{13}$$

Eq. (13) shows that the dimensionless temperature in the ballistic regime is a purely geometric quantity determined the probe transmissivity ratio. Interestingly, this ballistic dimensionless temperature profile is independent of the phonon dispersion relation for all geometries.

Similarly, in the ballistic regime, the heat flux expression in Eq. (12) simplifies to

$$q_{z,p} = (T_h - T_c) \frac{A_h}{A_p} \frac{\overline{Cv}}{4} \frac{\left(N_{hp,+} - N_{hp,-}\right)}{N}, \tag{14}$$

and the dimensionless heat flux defined in Eq. (7) becomes

$$Q = \frac{A_h}{A_p} \frac{\left(N_{hp,+} - N_{hp,-} \right)}{N} \,. \tag{15}$$

Here, N is the total number of phonon trajectories and $N_{hp,+}$ and $N_{hp,-}$ are the number of forward- and reverse-oriented trajectory crossings at the probe control surface. The dimensionless heat flux is also a purely geometric quantity in the ballistic regime, indicating that both θ_p and Q can be calculated once and for all for a given geometry and surface specularity. As we show below, these ballistic spatial profiles can provide insight into phonon transport behavior in patterned nanomaterials of experimental interest.

Lastly, we note that the ballistic results of Eqs. (13)–(15) are also appropriate to use for arbitrary bulk mean free paths if the material is assumed to be "gray", meaning that $\Lambda_{\rm bulk}$ is independent of ω and s.

Realistic materials are not well-described by this gray model because Λ_{bulk} depends strongly on ω for phonon-impurity and phonon-phonon scattering [14]. Despite this substantial shortcoming, the gray model is a convenient assumption for modeling and is used as a first step to understand the qualitative trends of heat conduction in materials as a function of nanostructure size or geometry [46]. In the more realistic non-gray and non-ballistic scenarios, Eqs. (6) and (11) should be used to quantify the heat flux and temperature profiles from phonon ray tracing calculations. In addition, it should be noted that the ray tracing approach is only strictly appropriate for the case of elastic scattering within the volume of the computational domain, as investigated below. Inelastic scattering mechanisms such as Umklapp scattering can only be treated approximately, in a manner that reproduces results given by the relaxation time approximation to the BTE. The phonon ray tracing approach cannot capture effects such as hydrodynamic phonon transport [47] that arise entirely due to interactions between phonons.

2.5. Heat flux error estimation

We evaluate the standard error in Q using a sub-sampling method [48]. To reduce the intrinsic statistical variance associated with the Monte Carlo method, we perform a large number of phonon trajectories $N \geq 5*10^5$. To perform the sub-sampling, these phonons are arbitrarily divided into J (here J=40) groups. For each group we obtained the averaged value of dimensionless heat flux Q_i (i=1,2,...,J). When J is large compared to unity (but small compared to N) and the results from each group are uncorrelated with one another, the standard error σ_Q of the heat flux calculation can be readily determined as

$$\sigma_{Q} = \sqrt{\frac{1}{J(J-1)} \sum_{i=1}^{J} (Q_{i} - Q)^{2}},$$
(16)

where $Q = \frac{1}{J} \sum_{i=1}^{J} Q_i$ is the mean heat flux calculated using the total number of simulated phonon trajectories. The 68% confidence interval is selected for evaluating the statistical uncertainty, and the standard error of the dimensionless heat flux is obtained from Eq. (16) as $(Q - \sigma_Q, Q + \sigma_Q)$.

3. Results

We first perform several validation studies to confirm that the ray tracing implementation captures the expected T and q profiles in benchmark geometries. Section 3.1 considers heat transfer in a fully dense system of length L, while Section 3.2 considers phonon transport along a square nanowire. Section 3.3 uses ray tracing to study the spatial profiles near a sharp constriction in a nanoslot geometry, while Section 3.4 investigates and optimizes the locally inverted T gradients observed in periodically etched nanomesh materials and Section 3.5 focuses on ballistic phonon focusing.

3.1. Validation: Fully dense material of length L

We first consider a fully dense (i.e., non-porous) material of length L. The material is implemented in our ray tracing calculations by separating the thermalizing hot and cold reservoir by a distance L along the z direction and applying specular boundary conditions along the x and y directions of the computational domain. Classical size effects on phonon transport in this geometry have been widely studied [45]. In the diffusive regime, the temperature gradient is linear with respect to z. In the ballistic regime, T is independent of position and there is a discontinuous temperature difference at the reservoir-device boundary.

Fig. 2(a) shows that our ray tracing simulations of the dimensionless temperature θ_p also display this expected behavior as a function of the dimensionless position z/L for a range of dimensionless mean free paths Λ/L . These calculations consider a gray phonon mean free path. Fig. 2(a)

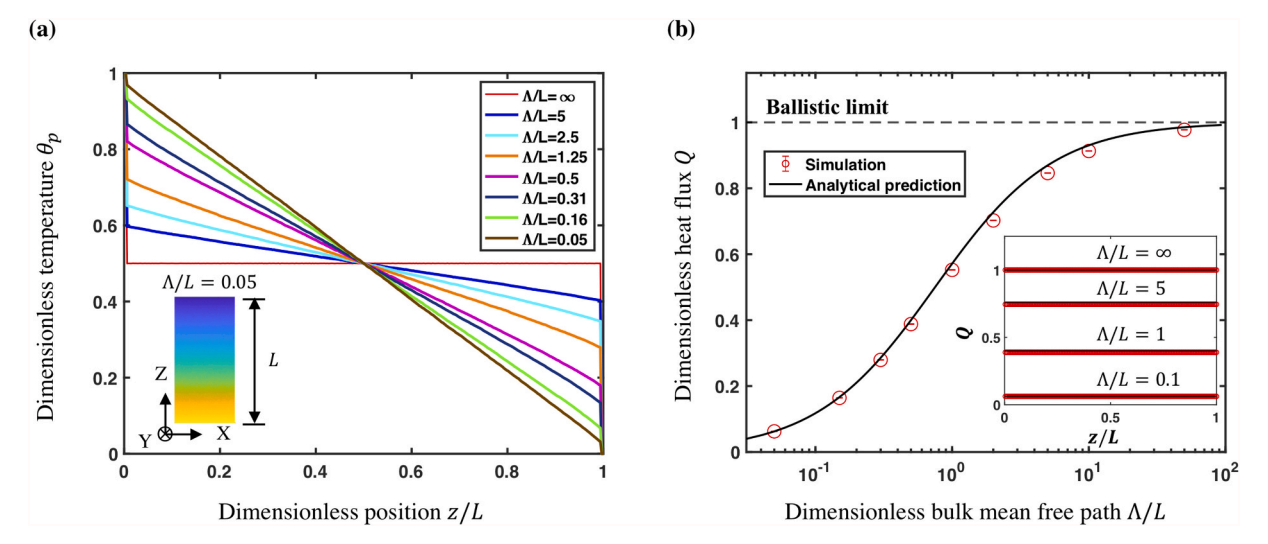


Fig. 2. Fully dense material validation. We validate the ray tracing mapping using a fully dense (i.e., non-porous) material of length L separating the hot and cold reservoir. (a) The dimensionless temperature profile $\theta_p(z)$ displays the expected behavior for eight values of the dimensionless gray mean free path Λ/L . The dimensionless temperature is $\theta_p = 0.5$ for all locations when $\Lambda/L = \infty$, while θ_p approaches the Fourier result of linear $\theta_p(z)$ at $\frac{\Lambda}{L} \ll 1$. θ_p is independent of x, as illustrated in the inset for $\Lambda/L = 0.05$. (b) Ray tracing results show that the dimensionless heat flux Q increases with increasing Λ/L and converge to the maximum value of unity in the fully ballistic limit. The simulation results (red circles) agree with a simple theoretical prediction (black line) using Mattheissen's rule. The inset shows that the heat flux distribution is independent of z/L for four values of Λ/L . as required from energy conservation.

shows that $\theta_p=0.5$ for all positions in the ballistic regime ($\Lambda/L=\infty$, red line), in agreement with the known ballistic limit [45]. As the dimensionless mean free path decreases, the temperature drop at the boundary also decreases in magnitude, and the temperature profile in the fully diffusive regime ($\Lambda/L\ll1$) approaches the linear Fourier prediction. The inset temperature profile in Fig. 2(a) for $\Lambda/L=0.05$ shows that θ_p is independent of the coordinate x, as expected.

Fig. 2(b) shows that the dimensionless heat flux Q calculated from ray tracing (points) increases with increasing Λ/L and converges to unity in the ballistic regime. In dimensional terms, this ballistic heat flux limit is given as $q_{\text{ball}} = \frac{\overline{CV}}{4}(T_h - T_c)$. Conservation of energy and symmetry arguments dictate that the heat flux is independent of z for all Λ/L , as verified in Fig. 2(b) inset for four values of Λ/L . To obtain the value of Q shown in the main plot of Fig. 2(b), we take the unweighted average value of Q obtained from all probe locations. Fig. 2(b) also compares the

ray tracing calculations of Q with a Matthiessen's rule prediction (line) using the effective phonon mean free path $\Lambda_{\rm eff} = \left(\Lambda^{-1} + \left(\frac{3L}{4}\right)^{-1}\right)^{-1}$. Here, Λ is the bulk mean free path and $\frac{3L}{4}$ is the boundary scattering mean free path for the fully dense material of length L. Once $\Lambda_{\rm eff}$ is known, Q_p can be calculated using the standard heat flux expression $q = \frac{1}{3}Cv\Lambda_{\rm eff}\left(\frac{\Delta T}{L}\right)$ and the nondimensionalization in Eq. (7), enabling direct comparison with the ray tracing results. The simulation results are in good agreement with this theoretical prediction, as shown in Fig. 2(b).

3.2. Validation: Square nanowire

As a second validation scenario, we consider transport along the axial direction of a square nanowire with side length w and length L. This nanowire geometry is a common system used to explore phonon mean

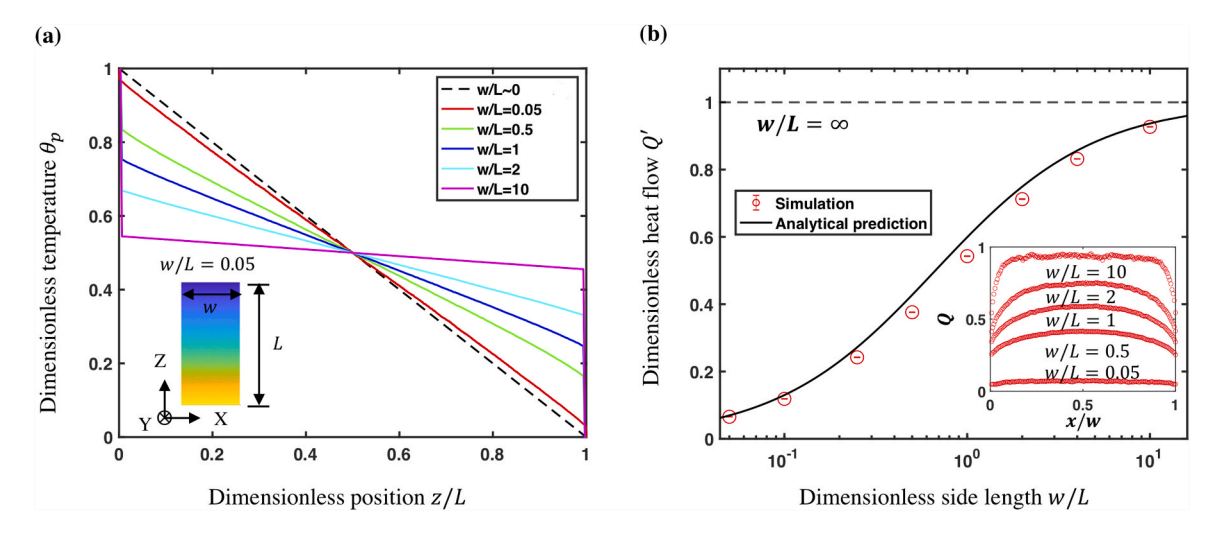


Fig. 3. Nanowire validation. (a) Fully ballistic $\theta_p(z)$ in a square nanowire of length L and side-length w (inset) with diffusely scattering surfaces. In the short-nanowire case where $w/L\gg 1$, ray tracing results approach the ballistic scenario from Fig. 2(a), while in the long-nanowire case $w/L\ll 1$, the ray tracing results for θ_p approach the Fourier limit (black dashed line). (b) The dimensionless heat flow Q' (found by averaging Q over the cross-sectional area) increases with increasing w/L and converges to unity at large w/L. The simulation results (red circles) are in good agreement with a simple Matthiessen's rule prediction (black line). The inset shows that the dimensionless heat flux Q depends on x for the nanowire, particularly when $w/L\gg 1$.

free path and thermal conductivity reductions due to boundary scattering [49]. In the case of fully diffuse scattering, BTE solutions show that the boundary scattering phonon mean free path of a long nanowire $(w/L\ll1)$ approaches 1.12w in the ballistic regime [20]. Fig. 3(a) shows the ray tracing calculation results for the diffuse surface nanowire temperature profile in the ballistic regime $(\Lambda/w=\infty)$ as a function of the dimensionless axial position z/L for a dimensionless side lengths w/L ranging from 0.05 to 10. The inset to Fig. 3(a) shows that the temperature profile is independent of x, as expected. In the short nanowire case where $w/L\gg1$, this nanowire geometry is identical to the scenario discussed in Section 3.1, and a large temperature drop near the reservoir is observed for w/L=10 (pink line, Fig. 3(a)). In the long nanowire case where $w/L\ll1$, the ray tracing θ_p profile for w/L=0.05 (red line) approaches the linear Fourier law prediction (black dashed line).

Fig. 3(b) shows the ray tracing calculations of the dimensionless heat flow $Q' \equiv \frac{1}{w^2} \int_0^w \int_0^w Q dx dy$ as a function of w/L. Though the temperature profile only depends on the axial direction, the heat flux Q is independent of z but depends on (x,y), as shown in Fig. 3(b) inset. The reduction in Q(x) observed in Fig. 3(b) inset is most pronounced for large w/L and arises from the scattering off the diffuse surfaces of the nanowire. The integrated heat flow Q' shown in Fig. 3(b) increases with increasing w/L and converges to unity in the short nanowire limit of $w/L\gg 1$. The ray tracing results are in good agreement with the simple Mattheissen's rule analytical approximation (black line) using the effective mean free path $\Lambda_{\rm eff} = \left(\left(\frac{3}{4} L \right)^{-1} + (1.12w)^{-1} \right)^{-1}$, again validating the ray tracing implementation. Here, $\frac{3L}{4}$ is the boundary scattering mean free path of a short nanowire, while 1.12w is the boundary scattering mean free path of a long square nanowire with diffusely scattering boundaries [20]. Our

calculations here do not include any bulk scattering and focus on diffuse nanowire surface scattering; if specular or partially specular surfaces are present, $Q_{\rm p}$ would be larger than in the diffuse scenario.

3.3. Nanoslot geometry

We now turn for the remainder of this manuscript to study transport in nanoporous materials. Fig. 4 focuses on phonon transport in a recently fabricated nanoslot geometry [50]. Prior work has shown that the total thermal resistance through the neck between the pores is sensitive to the ballistic transport, as commonly described using the Sharvin resistance expression [51]. Similarly, the temperature and heat flux distribution in the ballistic regime will also be affected by phonon backscattering at the pores. We implement this nanoslot geometry in the ray tracing calculations by considering a small neck between two diffusely scattering pores located between hot and cold reservoirs in the z direction, applying periodic boundary conditions along the x direction, and considering a specular scattering in the y direction. The dimensionless neck width in the x direction is 0.25 and the dimensionless pore width in the z direction is 0.1.

Fig. 4(a) shows θ_p for the nanoslot geometry in the fully ballistic regime $(\Lambda/L=\infty)$. Fig. 4(a) shows that the most obvious temperature gradients in the system are localized near the slot region at the neck between pores; this behavior is qualitatively similar to the diffusive results discussed below. In this ballistic regime, however, θ_p displays subtle line-of-sight effects that arise from the ray-like transport near the pore. Phonon trajectories passing through the neck region from hot to cold cannot reach the region just above the pore (e.g., near $\frac{z}{L}=0.6$ and $\frac{z}{L}=0.1$). At these regions, $\overline{\tau_{hp}}$ approaches 0 while $\overline{\tau_{cp}}$ is finite, leading to

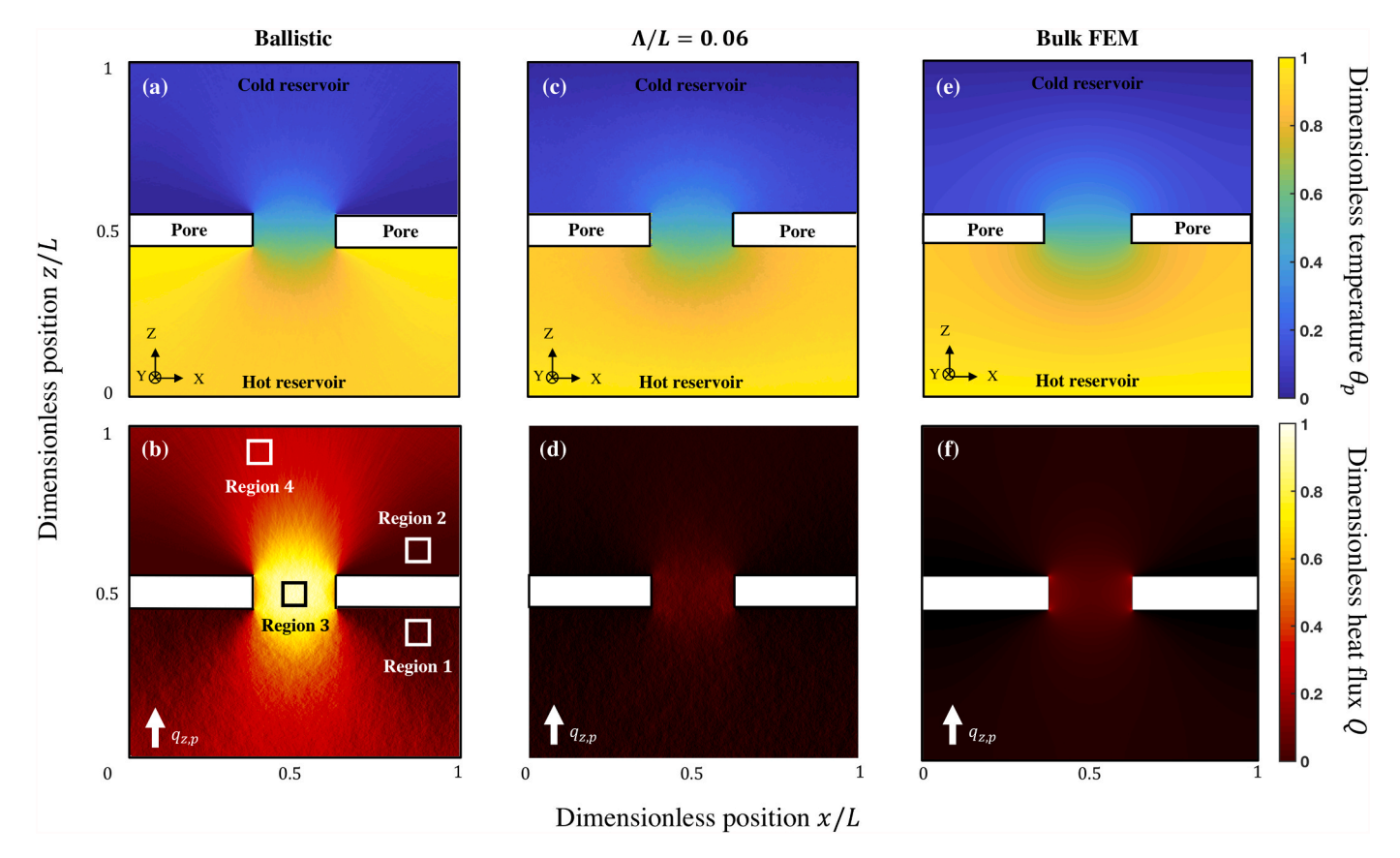


Fig. 4. Nanoslot geometry. (a) The ballistic temperature θ_p and (b) ballistic heat flux Q from ray tracing show sharp gradients at the region between pores and strong line-of-sight effects with shadowing near the pores. Heat flux trends in Regions (1)–(4) are discussed in the main text. (c) Diffusive θ_p and (d) diffusive Q profiles from ray tracing with a small dimensionless mean free path $\Lambda/L=0.06$. In this diffusive regime, θ_p does not display line-of-sight effects and Q is smaller in magnitude due to the intrinsic scattering. (e) Bulk finite-element method (FEM) results for θ_p and (f) Q the fully-diffusive regime are in good agreement with the ray tracing results from (c,d), further validating the ray tracing method.

 $\theta_p \approx 0$. Moving closer to the cold reservoir by increasing z/L at fixed x/L increases θ_p because phonon trajectories from the hot reservoir have a line of sight to the probe that is not blocked by the pores. A similar argument shows why the temperature just below the pore (e.g. at $\frac{z}{L}=0.4$ and $\frac{x}{L}=0.1$) is larger than the temperature closer to the hot reservoir.

Fig. 4(b) shows the ray tracing ballistic heat flux profile in the nanoslot geometry. This heat flux profile displays a heat flux concentration in the neck between the pores along with heat flux shadowing effects above and below the pores. Like all heat flux profiles shown in this work, Fig. 4(b) represents the dimensionless z component of the heat flux. The heat flux is symmetric about the midplane at z/L = 0.5, as expected. To gain further insight into the heat flux profiles and to interpret the results using the ray tracing formula of Eq. (15), we consider the boxes labeled Regions 1-4 in Fig. 4(b) and focus on phonon trajectories initialized from the hot reservoir at z/L=0. Region 1 is located just below a pore at $(\frac{x}{L}, \frac{z}{L}) = (0.9, 0.3)$, meaning that the phonon trajectories crossing through the region in the +z direction are likely to be backscattered by the pore and travel through the probe in the -zdirection. Referring to Eq. (15), this backscattering from the pore causes $N_{hp,-}$ to be quite similar to $N_{hp,+}$, leading to ultimate values of Q that are relatively small compared to the ballistic value of Q = 1. Similarly, Region 2 located above the pore at $(\frac{x}{t}, \frac{z}{t}) = (0.9, 0.7)$ also has a small value of Q near zero; this result can be interpreted by noting that the ballistic phonon trajectories from the hot reservoir are blocked by the pores and very few of these hot-reservoir phonon trajectories can be backscattering into Region 2, leading to both $N_{hp,+}$ and $N_{hp,-}$ values that are close to zero. Alternately, the Region 2 behavior could be justified by focusing on the trajectories initialized at the cold reservoir and using similar logic as applied to the hot-reservoir trajectories in Region 1, or by appealing to geometric and thermal symmetry in this linear response

Region 3 located in between the pores at $(\frac{x}{t}, \frac{z}{t}) = (0.5, 0.5)$ shows a local maximum value of Q that approaches unity; this local maximum arises because the phonon trajectories with a direct line of sight from the hot reservoir to the gap pass directly through the gap with no backscattering either before or after the gap, leading to $N_{hp,-}$ near zero and heat flow values that approach the scenario of Fig. 2. Lastly, Region 4 located at $(\frac{x}{I}, \frac{z}{I}) = (0.4, 0.9)$ close to the cold reservoir shows moderate values of Q that are larger than in the shadowed Regions 1 and 2 but smaller than in the mid-gap Region 3. At Region 4, the number of backscattered phonons from the hot reservoir $N_{hp,-}$ is still near zero, while $N_{hp,+}$ is smaller than in Region 3 because fewer hot-reservoir phonon trajectories have a direct line of sight to Region 4 than to Region 3. Overall, the ballistic temperature and heat flux mapping of Fig. 4 (a) and (b) provide further validation for the ray tracing results Eqs. (13) and (15), and shows that these ray tracing results can be interpreted in terms of the transmissivities and forward/reverse trajectories, respectively.

As noted above, the ray tracing calculations are most computationally efficient in the ballistic regime, and the majority of our attention therefore focuses on the ballistic behavior. However, it should be noted that the ray tracing equations can be used to model diffusive transport. To validate the ray tracing in the diffusive regime for the nanoslot geometry, Fig. 4(c) and (d) show θ_p and Q, respectively, calculated using a gray dimensionless mean free path $\Lambda/L=0.06$. The temperature profile in Fig. 4(c) displays the expected temperature gradient localization near the pore; however, as compared to the ballistic result of Fig. 4(a) and (c) displays no locally inverted temperature profile above or below the pores and no line-of-sight shadowing effects near the sharp pore edges. The diffusive heat flux profile in Fig. 4(d) displays a much smaller Q in the neck between pores than in the ballistic regime of Fig. 4(b), and this diffusive heat flux profile can be interpreted using the temperature gradients observed in Fig. 4(c) (i.e., regions with strong $\frac{d\theta_p}{dz}$ in Fig. 4(c) also display large Q in Fig. 4(d)). To compare the ray tracing method

with classical diffusive simulation of heat conduction, we also perform steady-state finite-element method (FEM) simulations using COMSOL Multiphysics on the same nanoslot geometry. To provide an analogous calculation to compare with the ray tracing predictions at $\frac{\Lambda}{L}=0.06$, the input FEM thermal conductivity is taken to be $k=\frac{1}{3}\overline{Cv}(0.06L)$; the particular value of \overline{Cv} is irrelevant for the dimensionless heat flow calculations shown here. Comparing Fig. 4(c) and (e), we see that the dimensionless temperature mapping is in good agreement with the FEM results, with an error of 5% in the temperature gradient along $\frac{\chi}{L}=0.5$ and within the region $\frac{z}{L}\in[0.4,0.6]$. The dimensionless heat flux mapping also has a <5% error between Fig. 4(d) and (f) when comparing the average Q value at the neck region $(x/L\in[0.45,0.55],z/L\in[0.375,0.625])$, confirming that the ray tracing method provides results that are consistent with Fourier heat conduction predictions when the phonon mean free paths are sufficiently small.

3.4. Nanomesh geometry

Fig. 5 shows our calculations of θ_p and Q for nanomesh geometries with different pore shapes (square, triangular, and circular) in the ballistic regime. These nanomesh structures are fabricated by etching holes through thin suspended membranes, and these nanomeshes have been used as model systems to explore phonon backscattering [12,22,52–55]. For all of the pore shapes shown in Fig. 5, we select periodic boundary conditions along the in-plane x direction and apply specular boundary conditions in the y direction to model a large-thickness nanomesh.

Fig. 5(a–c) showcases the unique features of the ballistic θ_p profiles in nanomesh geometries. To quantitatively compare these scenarios, Fig. 5 (d) displays a linecut of $\theta_p(z)$ at a x location that does not intersect a pore ($\frac{x}{L}=0.12$, dashed triangles and lines) and at a x location that does intersect a pore ($\frac{x}{L}=0.5$, solid triangles and lines). The dashed lines in Fig. 5(d) show that the temperature at the non-pore intersecting location $\theta_p(x/L=0.12,z)$ is continuous and monotonically decreases with increasing z, with the asymmetric triangular geometry displaying the smallest θ_p at all z. In contrast, the solid lines in Fig. 5(d) show that the pore-intersecting linecut at $\theta_p(x/L=0.5,z)$ displays a temperature that locally increases with increasing z within each region. This phenomenon has been previously observed and is referred to as a locally inverted temperature gradient [9,30,31,54].

This inverted temperature gradient can be visualized in Fig. 5(a) by contrasting the temperature gradients near surfaces 1 and 2 with the more typical temperature gradients in the non-intersecting pore regions. To compare the magnitude of the inverted temperature gradient effect between different geometries, we introduce a dimensionless temperature gradient

$$D = -\frac{\Delta\theta}{\Delta z/L},\tag{17}$$

where $\Delta\theta$ is the dimensionless temperature difference between the upper and lower pore at $\frac{x}{L}=0.5$ and $\Delta z/L$ is the dimensionless pore-pore distance at $\frac{x}{L}=0.5$, as illustrated schematically in Fig. 5(d). Negative values of D found from our ballistic calculations correspond to inverted temperature gradients, while positive values of D found from diffusive calculations are non-inverted and more traditionally observed in macroscopic systems.

We can readily interpret the inverted temperature gradient using the transmissivity ratio result of Eq. (13). In Fig. 5(a), the transmissivity from the hot reservoir to surface 1 $\overline{\tau_{h1}}$ is larger than the transmissivity from the hot reservoir to surface 2 $\overline{\tau_{h2}}$ because the regions near surface 2 are shadowed from hot-reservoir trajectories by the lower pore. Therefore, even though surface 2 is in closer proximity to the hot reservoir than surface 1, a thermalizing probe located near surface 1 would be more strongly coupled to the hot reservoir than a probe near surface 2, leading to the inverted temperature gradient phenomena. Similarly, if

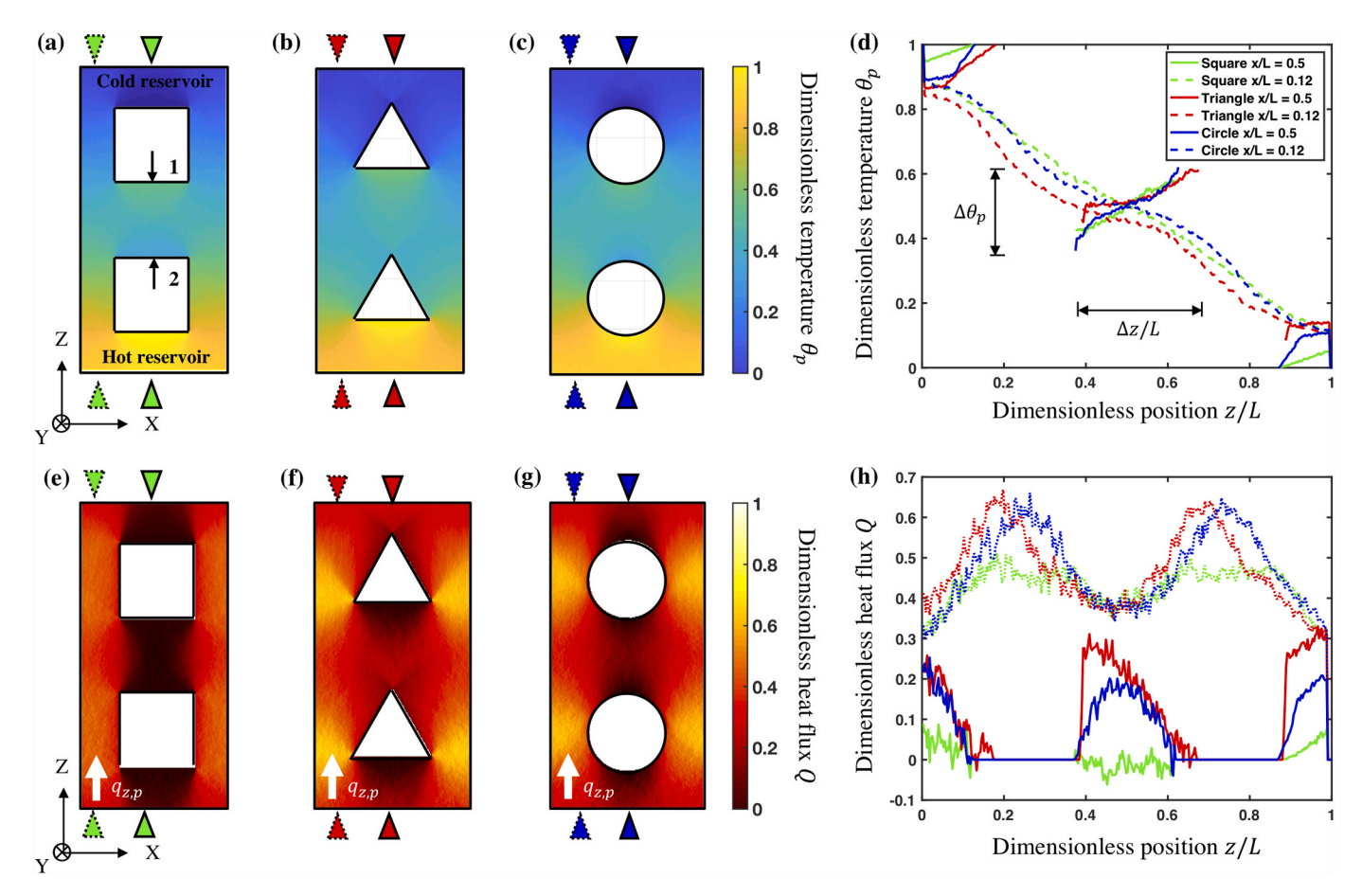


Fig. 5. Nanomesh mapping and inverted T gradient. Dimensionless θ_p mapping for (a) square, (b) triangular, and (c) circular pore nanomesh geometries in the ballistic limit. (d) Plots of $\theta_p(z)$ at two $\frac{\tau}{L}$ values (dashed and solid lines) show that all three pore shapes display an inverted temperature gradient [30,31], in which the direction of the local T gradients between the pores is locally inverted compared to the direction of global T differences between hot and cold reservoir. Referring to (a), this inverted gradient arises because phonon trajectories from the hot reservoir have a larger transmissivity to surface 1 than surface $\frac{\tau}{\tau_{h1}} = \frac{\tau_{h2}}{\tau_{h2}} = \frac{\tau_{h2}}{\tau_{h2}}$ due to shadowing of surface 1 by the lower pore. (e-g) The dimensionless heat flux Q(x,z) mapping and (h) Q(z) lineauts for two $\frac{\tau}{L}$ values shows that the heat flux is larger at $\frac{\tau}{L} = 0.12$ than at $\frac{\tau}{L} = 0.5$ due to phonon backscattering and pore shadowing. The circular pore heat flux in (g) is more similar to the triangular flux in (f) than the square pore scenario in (e).

we focused on the interactions with the cold reservoir, $\overline{\tau_{c2}} > \overline{\tau_{c1}}$, meaning that a probe near surface 2 would be more closely coupled to the cold reservoir temperature even though a probe located near surface 1 is physically closer to the cold reservoir.

The ray tracing simulations emphasize that the ballistic transport is the essential physics leading to the inverted temperature gradient, meaning that similar temperature profiles should also be observable in measurements of photon or electron transport. For photon calculations, this inverted T gradient can be calculated using geometric view factors [44] that are somewhat similar in concept to the phonon reservoir-probe transmissivities. The phonon transmissivity calculation directly includes all re-reflections from surfaces and is appropriate when internal surfaces are adiabatic, while the radiation view factors focus only on the direct line-of-sight view between diffuse surfaces and can be incorporated with both adiabatic and isothermal boundary conditions.

Fig. 5(e–g) compares the ballistic Q between the three pore geometries. Fig. 5(e) shows that the dimensionless heat flux in the square-pore nanomesh has values that are near zero at the inverted gradient regions located between the pores, while Q is larger and independent of position in the regions that are not blocked by pores. In the regions between pores, the strong phonon backscattering due the pore interactions causes $N_{hp,+}$ to be similar to $N_{hp,-}$, leading to small Q. The heat flux results for the triangular nanomesh in Fig. 5(f) show small values of Q in the regions directly beneath the pore surfaces that have surface normals in the z-drection, which is indicative of phonon backscattering. This triangular

nanomesh also displays a strong local maximum in Q in the regions that are adjacent to the pores without being shadowed by the pore. Lastly, the circular nanomesh results in Fig. 5(g) are more similar to the triangular pore as compared to the square pore, indicating that the square pore geometry displays the most efficient heat flux shadowing between pores in the ballistic regime. Fig. 5(h) quantifies this conclusion by comparing Q(z) of three cases along two linecuts at $\frac{x}{L} = 0.12$ (dashed) and $\frac{x}{L} = 0.5$ (solid). In all cases Q is larger at $\frac{x}{L} = 0.12$ than at $\frac{x}{L} = 0.5$, as expected. The heat flow at both $\frac{x}{t}$ locations more strongly on z for the triangle and circular pores than the square pores, because the square pores effectively confine the phonon trajectories near $\frac{x}{t} = 0.12$ for all z. As was the case in the nanoslot scenario discussed Section 3.3, the regions of the square pore with near-zero Q can be explained by the cases of Region 1 or 2 in Fig. 4(b), in the sense that either $N_{hp,+}$ is close to $N_{hp,-}$ due to backscattering or $N_{hp,+}$ and $N_{hp,+}$ are both near zero due to pore shadowing.

3.5. Inverted temperature gradient optimization in nanomesh

Fig. 6 uses ballistic ray tracing calculations to explore and optimize the inverted temperature gradient seen in Section 3.4. Section 3.4 focused on the case with two pores aligned in z, periodic boundary conditions in x, and infinite thickness in y. Fig. 6 expands this scope to study D in square and rectangular pore nanomesh structures with different geometric parameters and boundary conditions. We focus on

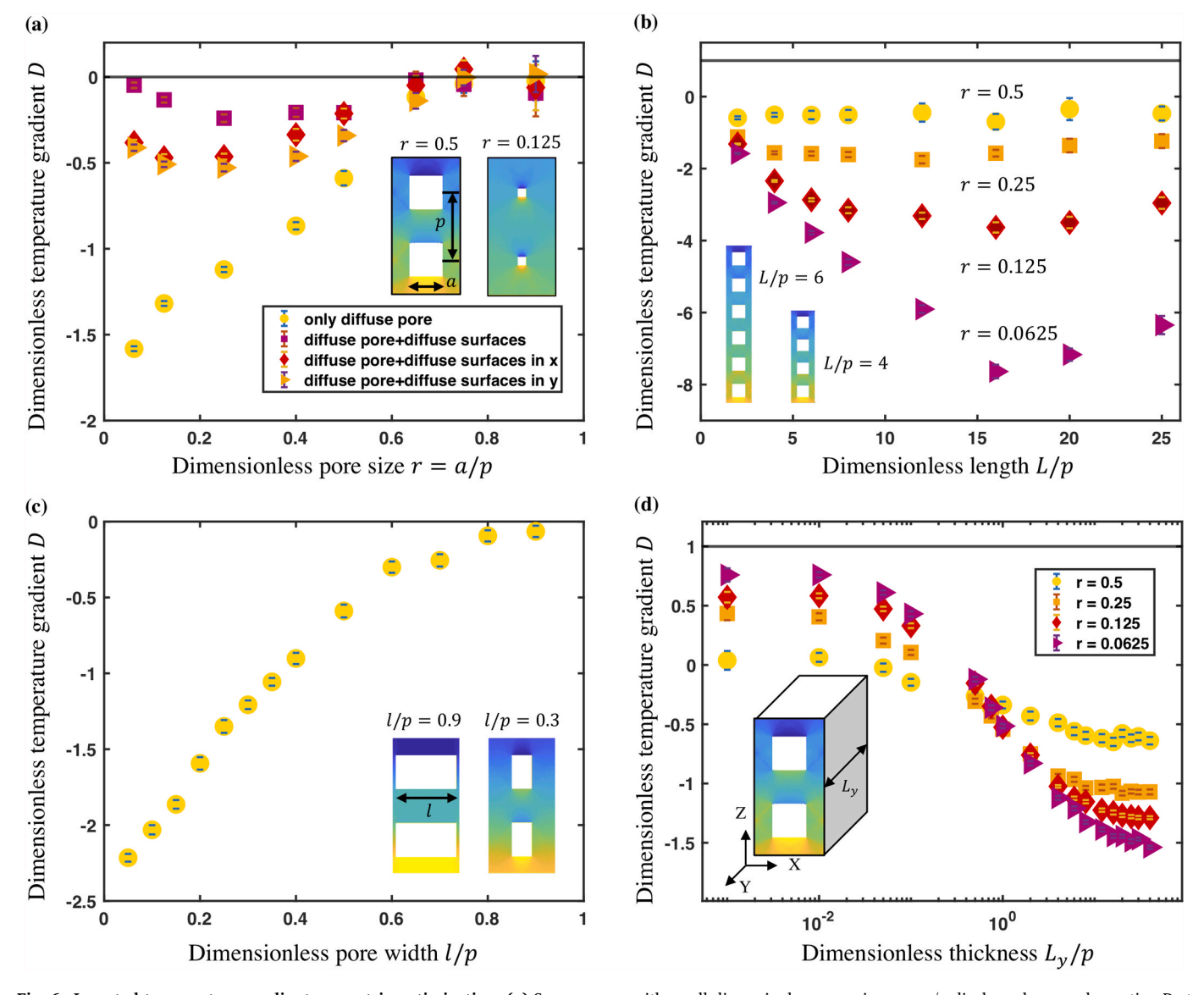


Fig. 6. Inverted temperature gradient geometric optimization. (a) Square pores with small dimensionless pore sizes r=a/p display a large and negative D at small r when the surrounding surfaces scatter phonon in a specular manner. Larger values of $r\sim 0.3$ lead to optimal D when one or both of the bounding surfaces scatter diffusely. In all cases D approaches zero in the large-pore scenario with r near unity. (b) D typically increases in magnitude with an increasing number of pores along the z-direction (i.e., increasing total length L/p. (c) Increasing the dimensionless pore width l/p decreases the magnitude of D due to reduction in the number of line-of-sight trajectories between the hot reservoir and lower surface of the upper pore. (d) Small thickness ratios L_y/p lead to undesirable positive D due to boundary scattering, while large L_y/p leads to negative D approaching the thick-film limit of (a) for $L_y/p\gg 1$.

square and rectangular pores in Fig. 6 because the square nanomesh in Fig. 5(a) displayed larger *D* than the circular or triangular pores. In all cases we consider diffuse phonon scattering from the pore, because the fabrication procedures for manufacturing nanoporous geometries typically induce roughness or oxidation at the pore edge at scales comparable to the phonon wavelengths [22].

Fig. 6(a) studies the effect of the dimensionless pore size r=a/p on D for four different boundary conditions in the x and y directions. Here, p is the pitch between pore centers in the z direction and a is the side-length of the square pore, as illustrated in Fig. 6(a) inset images for r=0.5 and r=0.125. Values of D that are large and negative correspond to strong deviations from typical diffusive behavior. For all boundary conditions, D approaches zero at large r because the large pores prevent direct line-of-sight phonon trajectories from the hot reservoir to the lower surface of the upper pore. The behavior at small r depends on the choice of boundary conditions. We first discuss the results for the "only diffuse pore" condition (yellow circles), in which specular boundaries are

applied in the x and y direction in a manner similar to Section 3.4. In this scenario, the largest magnitudes of D are observed at small r because phonons from the hot reservoir have a line-of-sight view to the bottom surface of the upper pore with minimal shadowing from the lower pore. In contrast, D approaches zero at small r in the scenario in which the bounding surfaces in the x and y directions $(L_x/p = 1 \text{ or } L_y/p = 1)$ scatter diffusely (red squares), leading to a local optimum in D for rranging from 0.2 – 0.4. Here, L_x is the width of the bounding surface in the x direction and L_y is the thickness in the out-of-plane y direction. This "diffuse pore and diffuse surfaces" scenario would be similar to a previously fabricated "nanoladder" geometry [56]. In this nanoladder case, D approaches zero at small r because phonons from the hot reservoir preferentially scatter from the bounding surfaces in x and y before reaching the pore surfaces. Because phonons from the cold reservoir also scatter off of these bounding surfaces, both the hot reservoir and cold reservoir phonon trajectories can reach both pore surfaces, causing D to approach zero. The observed D(r) when only one of the bounding surfaces scatter diffusely (orange triangles and diamonds) are similar to each other and have smaller magnitude of D at small r, as in the nanoladder scenario.

Fig. 6(b) considers the effects of increasing the number of pores along the direction of transport while considering periodic boundary conditions in the x direction and specular scattering in the y direction. These results would be relevant for nanomesh experiments that utilize periodically repeating pore structures in the x and z direction. We select an even number of pores for the system and calculate D between the two middle pores along the z direction, following the same procedure shown in Fig. 5(d). Fig. 6(b) shows that D does not vary strongly with the dimensionless length L/p for r=0.5 (yellow circles) and r=0.25 (orange squares), indicating that the two-pore results from Fig. 6(a) are appropriate even for large lengths. In contrast, the magnitude of D increases with increasing L/p for r=0.125 (red diamonds) and r=0.0625 (magneta triangles) before saturating at lengths $L/p > r^{-1}$. At a given L/p

p, the magnitude of D increases with decreasing r, as seen for the diffuse pore scenario in Fig. 6(a).

Fig. 6(c) considers the pore-shape effect by varying the dimensionless pore width l/p of a two-rectangular pore system at fixed dimensionless pore side length of 0.5. The boundaries along the x and y directions are set to be specular. In agreement with the general trends from Fig. 6(a), increasing the pore width reduces the magnitude of D. This trend is due to the increased shadowing and reduction in the line-of-sight interactions between the hot reservoir and the lower surface of the upper pore at large l/p. For the parameters shown here, D scales linearly with l/p for l/p ranging from 0 to 0.5, indicating that narrow pore widths are desirable for enhanced D. Lastly, Fig. 6(d) considers the effect of diffuse scattering at the finite y-thickness surface for four values of square pore size ratio r and periodic boundary conditions in the x direction. Experimental nanomeshes are typically fabricated using lithography and etching of thin suspended silicon membranes [22,55],

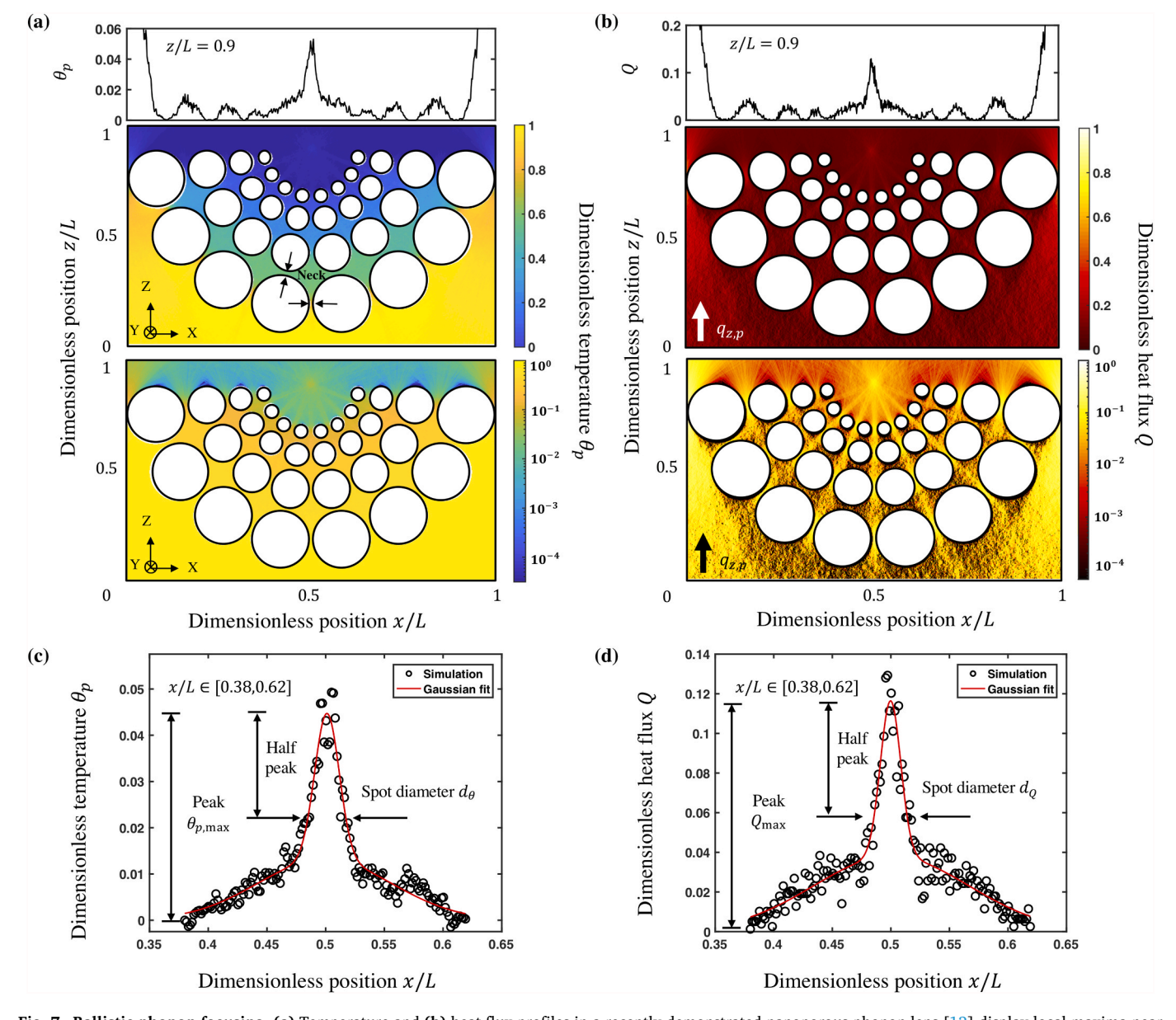


Fig. 7. Ballistic phonon focusing. (a) Temperature and (b) heat flux profiles in a recently demonstrated nanoporous phonon lens [12] display local maxima near the focal point of the lens. The four rows of eight circular pores per row are aligned such that phonon trajectories are preferentially channeled to the focal point after travelling between the necks separating the pores. The top panel in (a,b) shows the x-dependence of θ_p and Q along z/L=0.9, while the middle and bottom panels display the linear and logarithmic scaled colormaps to demonstrate the phonon trajectory focusing. (c,d) We used dual Gaussian equation to fit the simulation results located between $x/L \in [0.38, 0.62]$, and define the local maximum value as $\theta_{p,max}$ and Q_{max} and the full-width half-max diameter of the focal spot (d_θ, d_Q) .

meaning that the thickness is not necessarily large compared to the pitch. Fig. 6(d) shows that the inverted temperature gradients for a two-pore system are only observed for thickness ratios L_v/p that are large compared to unity. At thickness ratios that are small compared to unity, the phonon scattering from the diffuse membrane surfaces in y leads to positive D. At very small L_y/p compared to unity, D approaches a thickness-independent value for all r that matches the diffusive limit prediction using Fourier's law. At large L_v/p , D is negative valued and approaches the infinite-thickness case shown in Fig. 6(a) for all r values shown here. The effect of introducing bulk scattering in the volume of the membrane would have a qualitatively similar effect to the film-thickness dependent study shown here, as both bulk scattering and diffuse film-surface scattering force the temperature and heat flux profiles towards the diffusive limit. Overall, the analysis of Fig. 6 indicates that the periodic nanomesh geometry with square pores, small-to-moderate r, and large membrane thickness is a promising experimental platform to investigate inverted temperature gradients.

3.6. Ballistic phonon focusing using geometric lensing

Fig. 7 shows our ray tracing calculations of a ballistic phonon lens. This lens uses phonon line-of-sight trajectories through an array of pores to generate locally concentrated heat fluxes and temperatures near the focal point. This concept of ballistic phonon lensing in nanoporous silicon membranes was introduced and experimentally fabricated by Anufriev et al. in 2017 [32]. This work also performed Monte Carlo BTE calculations to determine the steady-state temperature and heat flux profiles for the experimental geometries. The goal of our study is to demonstrate that the ray tracing also reproduces the known phonon focusing effect, and to explore the geometry-dependent focusing capabilities of the ballistic lens. Our nondimensional calculations also emphasize that the lens behavior is a purely geometric quantity in the ballistic regime, meaning that the results are not restricted to silicon nanomaterials.

Fig. 7(a and b) show θ_p and Q for a ballistic phonon lens with four aligned rows, each row consisting of eight circular pores arranged at a constant radial distance from the focal point at $\left(\frac{x}{t},\frac{z}{t}\right)=(0.5,0.9)$. In these calculations, the surfaces of the pores are diffuse and the membrane thickness is assumed to be infinite. The upper row shows a focal plane line profile as a function of x/L through the focal point at z/L =0.9, while the middle and lower rows are colormaps that visualize the results in linear and logarithmic scales, respectively. Both the θ_p and Qmapping show a local maximum at the focal point, as seen in the linecuts in the top row. For this geometry, the focal point in the Q profiles of Fig. 7(b) is visible both in the linear and logarithmic scales, while the local maximum in θ_p is most apparent in the logarithmic scale of Fig. 7 (a). The local maxima in θ_p seen in the top row of Fig. 7(a) occurs because phonons have a direct line of sight from the hot reservoir to the focal point through the neck regions between the pores, which enhances $\tau_{\rm hp}$ at the focal point as compared to the other x locations in the focal plane at z/L = 0.9. The temperature profile in Fig. 7(a) shows sharp decreases in θ_p at each concentric ring of pores because phonons from hot reservoir are backscattered by the pores. Because the circular pores in different rows of the lens are aligned, the phonons trajectories passing through the necks between pores will converge near the focal point. If the pores in different rows were staggered instead of aligned (not shown), the focusing phenomena is not observed. Similarly, the heat flux profiles in Fig. 7(b) show strong focusing effects at the focal plane due to the imbalance between forward- and reverse-crossing phonon trajectories. The line-cut profiles of θ_p and Q in the top rows of Fig. 7(a) and (b), respectively, show secondary maxima along either side of the primary focal peak. These secondary peaks do not arise from phonon diffraction (which is not included in these ray tracing calculations) but instead arise from phonons that scatter off of a pore surface and are channeled in the continuous solid regions between the rows of pores.

To quantify the peak temperature and heat flux values $(\theta_{p,\max},Q_{\max})$ and the focal diameters (d_{θ},d_Q) , we fit the ray tracing results at z/L=0.9 with the dual Gaussian equation $f(x)=a_1\exp\left(-\left(\frac{x-b_1}{c_1}\right)^2\right)+a_2\exp\left(-\left(\frac{x-b_1}{c_1}\right)^2\right)$

 $\left(-\left(\frac{x-b_2}{c_2}\right)^2\right)$ within the range of $x/L \in [0.38,0.62]$; here a_1,b_1 c_1,a_2,b_2 and c_2 are fitting parameters. Fig. 7(c) and (d) show that this dual Gaussian fit (red lines) accurately captures the ray tracing results (black points) for the temperature and heat flux profiles, respectively. The focal diameter in the x-direction (d_θ,d_Q) is defined as the full-width at half maximum of the fitting function, as labeled in Fig, 7(c) and (d). In this scenario, the dimensionless diameter $d_\theta=0.054$ and $d_Q=0.044$ are not identical. Here we only consider the diameter (d_θ,d_Q) along x direction at z/L=0.9, but note that the focal point is approximately circular, meaning that similar z-direction focal point lengthscales are obtained.

Fig. 8 studies geometry-dependent focusing for θ_n and Q as a function of the dimensionless pore size $\varepsilon = b/\Omega_a$, where b is the pore diameter within a row and Ω_a is the arc length between the centers of two pores within a row. To illustrate this definition, the Fig. 8(c) inset shows the schematic of the first row of eight pores with a row radius R. The arc length between pores is $\Omega_a = \pi R/8$, and the pore diameter b must be smaller than Ω_a to avoid pore intersection. This dimensionless pore diameter ε is constant for all rows of pores; since each row has a different R but still has eight pores, the pore diameters and minimum distances between pores increase with increasing R. The geometry shown in Fig. 7 has $\varepsilon = 0.4$. Returning to Fig. 8, the colormaps in Fig. 8(a) and (b) show that both the peak magnitude and the size of the focal spot decrease with increasing ε for both the θ_p and Q profiles, respectively. This result is easily interpreted: in the limiting case of a vanishing pore diameter $(\varepsilon \rightarrow 0)$, the intensity is large but there is no focal spot. In the limiting case of a small neck between pores $(\varepsilon \rightarrow 1)$, strong phonon backscattering from the pores decreases the phonon transmission and intensity, but phonons that do transmit through the narrow line-of-sight lead to a small focal diameter.

Fig. 8(c) quantifies the decrease in the peak values $\theta_{p,max}$ and Q_{max} (left, blue) and spot diameters d_{θ} and d_{Q} (right, red), for the temperature and heat flux as a function of ε . The focal spot diameters are fairly similar between the heat flux (asterisks) and temperature profile (circle) results when $\varepsilon > 0.7$, while the dimensionless peak values differ by as much as a factor of two between heat flux and temperature at fixed ε . In all cases, the peak values and spot diameters are most sensitive to ε for ε larger than 0.2 and depend less strongly on ε for ε very small compared to unity. One possible figure of merit summarizing both the peak value and the spot size effects would be the peak value normalized by a representative focal diameter. Fig. 8(d) shows that this dimensionless spot ratio for the temperature profile $\theta_{\rm p,max}/d_{\theta}$ (purple square) and for the heat flux profile Q_{max}/d_{Q} (yellow triangle) decrease weakly with increasing ε . This result indicates that changing ε causes both the peak values $\theta_{p,\max}$ and Q_{\max} and the focal diameters d_{θ} and d_{Q} to decrease in a fairly similar manner (see Fig. 8(c) also). The overall dimensionless spot ratio for heat flux is approximately a factor of two larger than the temperature spot ratio, which agrees with the magnitude of peak values shown in Fig. 8(c). Though outside the scope of this work, future research exploring geometric heat focusing to optimize the pore shape, pore distribution, or number of focal points of could be useful in the future experimental exploration of ballistic phonon focusing. This current work emphasizes that modifications to the geometry which decrease the focal diameter will also act to decrease the magnitude of the temperature or heat flux at the spot.

Lastly, Fig. 9 investigates the effect of bulk scattering on the phonon focusing. We performed ray tracing calculations for the lens geometry with dimensionless pore size $\varepsilon=0.6$ and dimensionless mean free paths Λ/L ranging from 10^{-1} to 10^3 . Here, L is the full width of the lensfocusing array in the x direction, as defined in Fig. 7(a). The colormaps in Fig. 9(a) and (b) show the temperature and heat flux profiles,

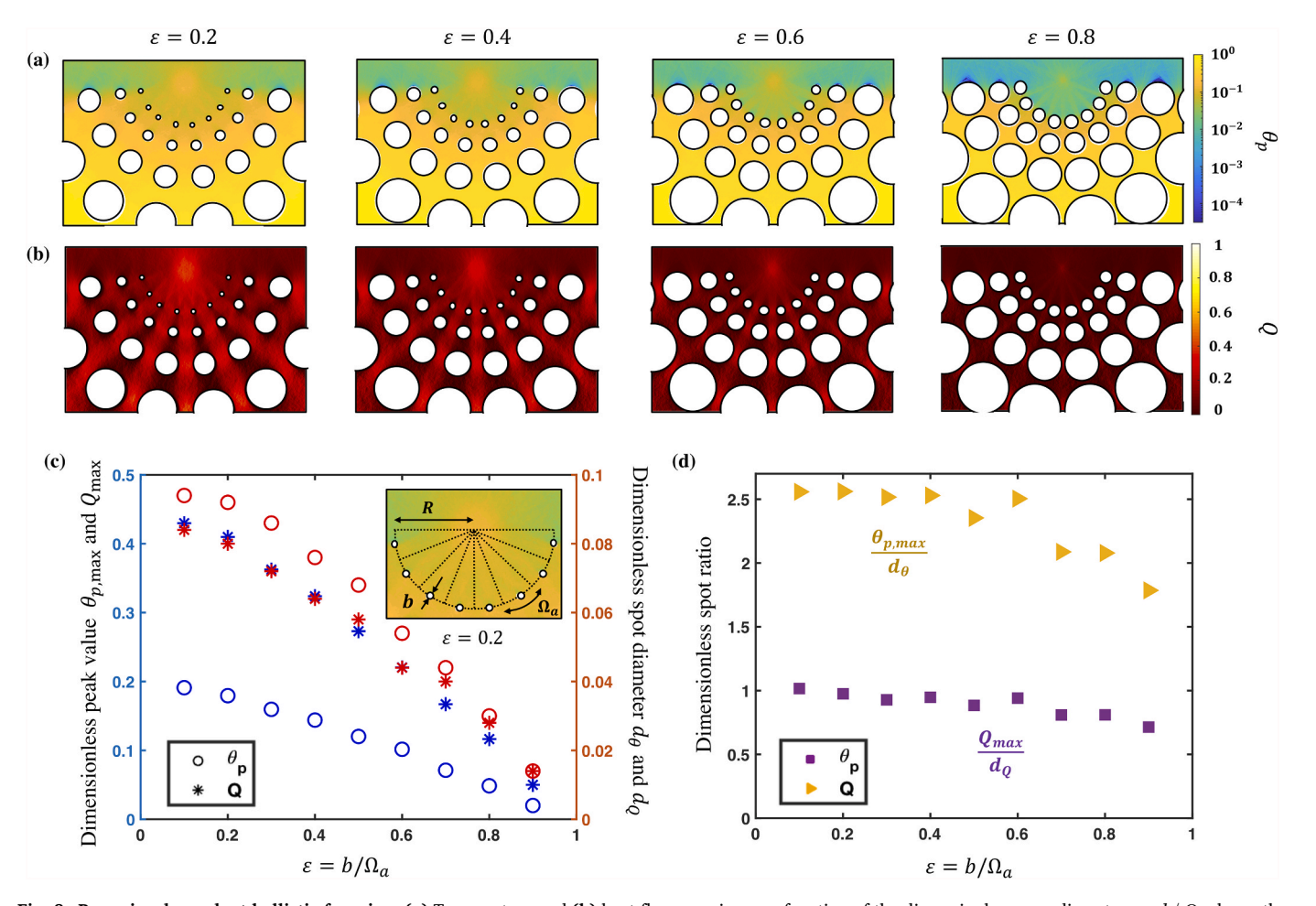


Fig. 8. Pore-size dependent ballistic focusing. (a) Temperature and (b) heat flux mapping as a function of the dimensionless pore diameter $\varepsilon = b/\Omega_{\rm a}$ shows the evolution in the focal point for different pore sizes. Here, the pore diameter b and arc-length $\Omega_{\rm a}$ are illustrated in the (c) inset for the first row of pores. (c) As ε increases, the peak values $\theta_{p,\max}$ or Q_{\max} (left) and the focal spot diameters d_{θ} or d_{Q} (right) decrease monotonically due to the smaller neck size between pores. (d) The spot ratio $\theta_{p,\max}/d_{\theta}$ and Q_{\max}/d_{Q} do not show a strong dependence on ε , indicating the change of ε impacts the peak values $\theta_{p,\max}$ and Q_{\max} and the focal spot diameters d_{θ} and d_{Q} in a similar manner.

respectively, for $\Lambda/L=10$ (left), $\Lambda/L=1$ (center), and $\Lambda/L=0.1$ (right). As expected, the ray tracing results for $\Lambda/L = 10$ display focusing results that are qualitatively similar to the ballistic results shown in the third column of Fig. 8(a) and (b). As the dimensionless mean free path decreases, the diffusive scattering in the material decreases the magnitude of the temperature rise and heat flux near the focal spot, as seen most clearly in the ray tracing results for $\Lambda/L\,=\,0.1$. Within the ray tracing methodology, this reduction in the focal spot intensity arises due to the reduction in the phonon transmission coefficient from the hot reservoir to the focal spot. Fig. 9(c) further quantifies this reduction by showing that the peak temperature value $\theta_{p,max}$ (circles) and peak heat flux $Q_{\rm max}$ (stars) decrease with decreasing Λ/L . These peak values saturate at the ballistic limit of $\theta_{p,max} = 0.09$ and $Q_{\rm max}=0.22$ for all $\Lambda/L>10$, but are reduced to $\theta_{\rm p,max}=0.03$ and $Q_{\rm max}=0.05$ for $\Lambda/L=0.1$. Similarly, Fig. 9(d) shows that introducing bulk scattering increases the focal spot diameters for the temperature profile d_{θ} (circles) and the heat flux profile d_{Q} (stars). This increase in the focal spot size arises because bulk scattering leads to diffusion, dispersing the phonon trajectories away from the focal spot. Further calculations that properly consider the phonon frequency-dependent scattering rates would be required to quantify the phonon focusing observed in realistic phonon lenses. However, these results show that the strongest phonon focusing effects will be observed when the mean free path is substantially larger than the dimensions of the pore array, but that mild focusing effects can be observed even when mean free paths

are comparable to or slightly smaller than the pore array dimensions.

4. Summary

We describe a phonon Monte Carlo ray tracing method to calculate the local temperature and heat flux, with a particular focus on ballistic phonon transport in nanostructures. The advantage of the ray tracing technique compared to the traditional BTE approach is that the full phonon distribution function does not need to be evaluated at each location, and the phonon trajectories can be computed in parallel. The derivation also provides a simple interpretation of the temperature profile in terms of a weighted transmissivity ratio between reservoirs and thermalizing probes, and an interpretation of the heat flux in terms of the imbalance between forward and reverse phonon trajectory crossings at a control surface. We validated the ray tracing method for benchmark dense material, nanowire, and nanoslot geometries. Our study of the dimensionless inverted temperature gradient D in nanomesh structures found that smaller pores, thick films, and multiple pores along the direction of transport lead to large and negative values of D in the ballistic regime. Our application of the ray tracing method to study ballistic phonon lensing in porous structures found that increasing the dimensionless pore size decreases the spot size and the peak amplitudes of the temperature and heat flux profiles in the focal spot. In summary, our ray tracing method can be used to probe ballistic phonon transport physics and design nanostructures with unusual temperature and heat

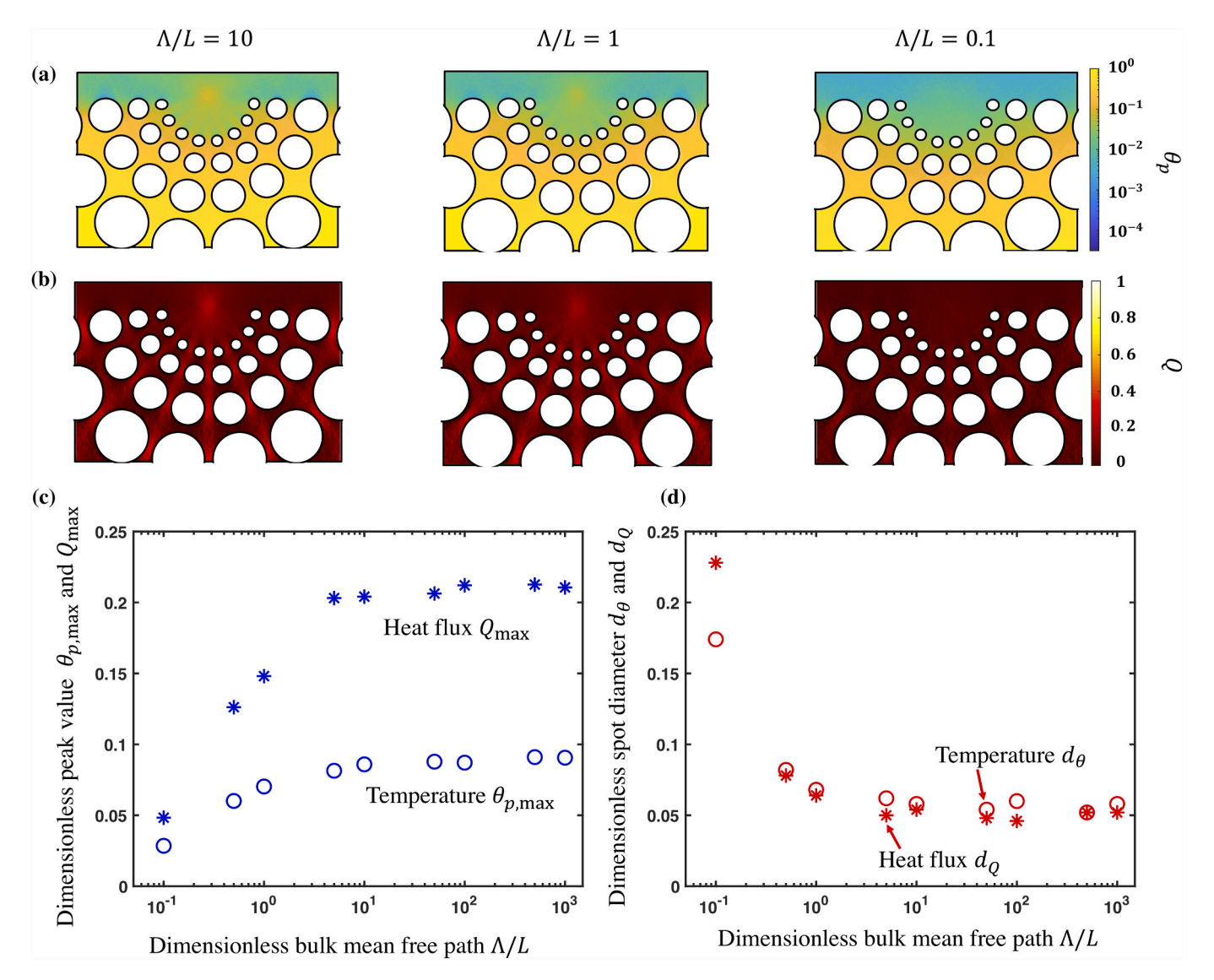


Fig. 9. Mean free path-dependent focusing. (a) Temperature and (b) heat flux maps as a function of the dimensionless bulk mean free path Λ/L for fixed dimensionless pore size $\varepsilon = 0.6$. Here, L is the full-width of the pore array, as introduced in Fig. 7. (c) The dimensionless peak values $\theta_{p,max}$ (circles) and Q_{max} (stars) decrease with decreasing Λ/L , showing that the lensing is present at Λ/L of order unity but maximized in the ballistic regime. (d) Similarly, the spot diameters d_θ and d_Q increase with decreasing Λ/L because the diffusive scattering eliminates the ray-like phonon focusing.

flux gradients in the ballistic regime.

Credit author statement

Yingru Song: Methodology, Software, Investigation, Writing-Original Draft. **Geoff Wehmeyer**: Conceptualization, Methodology, Writing: Review and Editing.

Declaration of competing interest

The authors declare that they have no known competing financial interests or personal relationships that could have appeared to influence the work reported in this paper.

Data availability

Data will be made available on request.

Acknowledgements

This work was supported by a grant from the Welch Foundation (Grant No. C-2023) and a grant from the National Science Foundation (Grant No. CBET-2145461).

References

- [1] D.G. Cahill, P.V. Braun, G. Chen, D.R. Clarke, S. Fan, K.E. Goodson, P. Keblinski, W. P. King, G.D. Mahan, A. Majumdar, Nanoscale thermal transport. II. 2003–2012, Appl. Phys. Rev. 1 (1) (2014): 011305.
- [2] D.G. Cahill, W.K. Ford, K.E. Goodson, G.D. Mahan, A. Majumdar, H.J. Maris, R. Merlin, S.R. Phillpot, Nanoscale thermal transport, J. Appl. Phys. 93 (2) (2003) 703-818
- [3] A.M. Marconnet, M.A. Panzer, K.E. Goodson, Thermal conduction phenomena in carbon nanotubes and related nanostructured materials, Rev. Mod. Phys. 85 (3) (2013) 1295.
- [4] G. Chen, Nanoscale Energy Transport and Conversion: A Parallel Treatment of Electrons, Molecules, Phonons, and Photons, Oxford University Press, 2005.
- [5] D.P. Sellan, E.S. Landry, J. Turney, A.J. McGaughey, C.H. Amon, Size effects in molecular dynamics thermal conductivity predictions, Phys. Rev. B 81 (21) (2010): 214305.

- [6] W. Zhang, T. Fisher, N. Mingo, The atomistic Green's function method: an efficient simulation approach for nanoscale phonon transport, Numer. Heat Tran., Part B: Fund. 51 (4) (2007) 333–349.
- [7] A. Minnich, Advances in the measurement and computation of thermal phonon transport properties, J. Phys. Condens. Matter 27 (5) (2015): 053202.
- [8] L. Lindsay, First principles peierls-Boltzmann phonon thermal transport: a topical review, Nanoscale Microscale Thermophys. Eng. 20 (2) (2016) 67–84.
- [9] M.S. Jeng, R. Yang, D. Song, G. Chen, Modeling the thermal conductivity and phonon transport in nanoparticle composites using Monte Carlo simulation, J. Heat Tran. 130 (4) (2008): 042410.
- [10] G. Romano, K. Esfarjani, D.A. Strubbe, D. Broido, A.M. Kolpak, Temperature-dependent thermal conductivity in silicon nanostructured materials studied by the Boltzmann transport equation, Phys. Rev. B 93 (3) (2016): 035408.
- [11] G. Romano, J.C. Grossman, Heat conduction in nanostructured materials predicted by phonon bulk mean free path distribution, J. Heat Tran. 137 (7) (2015): 071302.
- [12] N.K. Ravichandran, A.J. Minnich, Coherent and incoherent thermal transport in nanomeshes, Phys. Rev. B 89 (20) (2014): 205432.
- [13] D. Ding, X. Chen, A. Minnich, Radial quasiballistic transport in time-domain thermoreflectance studied using Monte Carlo simulations, Appl. Phys. Lett. 104 (14) (2014): 143104.
- [14] K.T. Regner, D.P. Sellan, Z. Su, C.H. Amon, A.J. McGaughey, J.A. Malen, Broadband phonon mean free path contributions to thermal conductivity measured using frequency domain thermoreflectance, Nat. Commun. 4 (1) (2013) 1640.
- [15] J.-P.M. Péraud, C.D. Landon, N.G. Hadjiconstantinou, Monte Carlo methods for solving the Boltzmann transport equation, Ann. Rev. Heat Tran. 17 (2014).
- [16] J.-P.M. Péraud, N.G. Hadjiconstantinou, Efficient simulation of multidimensional phonon transport using energy-based variance-reduced Monte Carlo formulations, Phys. Rev. B 84 (20) (2011): 205331.
- [17] J. Schleeh, J. Mateos, I. Íñiguez-de-la-Torre, N. Wadefalk, P.-A. Nilsson, J. Grahn, A. Minnich, Phonon black-body radiation limit for heat dissipation in electronics, Nat. Mater. 14 (2) (2015) 187–192.
- [18] S. Wolf, N. Neophytou, H. Kosina, Thermal conductivity of silicon nanomeshes: effects of porosity and roughness, J. Appl. Phys. 115 (20) (2014): 204306.
- [19] D. Chakraborty, S. Foster, N. Neophytou, Monte Carlo phonon transport simulations in hierarchically disordered silicon nanostructures, Phys. Rev. B 98 (11) (2018): 115435.
- [20] T. Hori, J. Shiomi, C. Dames, Effective phonon mean free path in polycrystalline nanostructures, Appl. Phys. Lett. 106 (17) (2015): 171901.
- [21] K.D. Parrish, J.R. Abel, A. Jain, J.A. Malen, A.J.H. McGaughey, Phonon-boundary scattering in nanoporous silicon films: comparison of Monte Carlo techniques, J. Appl. Phys. 122 (12) (2017): 125101.
- [22] J. Lee, W. Lee, G. Wehmeyer, S. Dhuey, D.L. Olynick, S. Cabrini, C. Dames, J. J. Urban, P.D. Yang, Investigation of phonon coherence and backscattering using silicon nanomeshes. Nat. Commun. 8 (2017): 14054.
- [23] Y. Song, G. Wehmeyer, Maximizing and minimizing the boundary scattering mean free path in diameter-modulated coaxial cylindrical nanowires, J. Appl. Phys. 130 (4) (2021): 045104.
- [24] Y. Zeng, A. Marconnet, Reevaluating the suppression function for phonon transport in nanostructures by Monte Carlo techniques, J. Appl. Phys. 125 (3) (2019): 034301
- [25] C. Shao, T. Hori, J. Shiomi, P-TRANS: a Monte Carlo ray-tracing software to simulate phonon transport in arbitrary nanostructures, Comput. Phys. Commun. 276 (2022): 108361.
- [26] T. Hori, Role of geometry and surface roughness in reducing phonon mean free path and lattice thermal conductivity of modulated nanowires, Int. J. Heat Mass Tran. 156 (2020): 119818.
- [27] D. Chakraborty, H. Karamitaheri, L. de Sousa Oliveira, N. Neophytou, Effect of wave versus particle phonon nature in thermal transport through nanostructures, Comput. Mater. Sci. 180 (2020): 109712.
- [28] V. Mishra, J.E. Garay, C. Dames, Leveraging anisotropy for coupled optimization of thermal transport and light transmission in micro-structured materials for highpower laser applications, Adv. Theory Simulat. 3 (9) (2020): 2000036.
- [29] J. Maire, R. Anufriev, T. Hori, J. Shiomi, S. Volz, M. Nomura, Thermal conductivity reduction in silicon fishbone nanowires, Sci. Rep. 8 (2018) 4452.
- [30] Q. Hao, G. Chen, M.S. Jeng, Frequency-dependent Monte Carlo simulations of phonon transport in two-dimensional porous silicon with aligned pores, J. Appl. Phys. 106 (11) (2009): 114321.

- [31] R. Yang, G. Chen, Thermal conductivity modeling of periodic two-dimensional nanocomposites, Phys. Rev. B 69 (19) (2004): 195316.
- [32] R. Anufriev, A. Ramiere, J. Maire, M. Nomura, Heat guiding and focusing using ballistic phonon transport in phononic nanostructures, Nat. Commun. 8 (2017): 15505
- [33] A. Reihani, Y. Luan, S. Yan, J.W. Lim, E. Meyhofer, P. Reddy, Quantitative mapping of unmodulated temperature fields with nanometer resolution, ACS Nano 16 (1) (2021) 939–950.
- [34] D. Jaque, F. Vetrone, Luminescence nanothermometry, Nanoscale 4 (15) (2012) 4301–4326.
- [35] G. Wehmeyer, K.C. Bustillo, A.M. Minor, C. Dames, Measuring temperature-dependent thermal diffuse scattering using scanning transmission electron microscopy, Appl. Phys. Lett. 113 (25) (2018): 253101.
- [36] M. Mecklenburg, W.A. Hubbard, E. White, R. Dhall, S.B. Cronin, S. Aloni, B. Regan, Nanoscale temperature mapping in operating microelectronic devices, Science 347 (6222) (2015) 629–632.
- [37] B. Yang, G. Chen, Partially coherent phonon heat conduction in superlattices, Phys. Rev. B 67 (19) (2003): 195311.
- [38] S. Mazumder, A. Majumdar, Monte Carlo study of phonon transport in solid thin films including dispersion and polarization, J. Heat Tran. 123 (4) (2001) 749–759.
- [39] S.G. Das, A. Dhar, Landauer formula for phonon heat conduction: relation between energy transmittance and transmission coefficient, Eur. Phys. J. B 85 (11) (2012) 372.
- [40] C. Jeong, S. Datta, M. Lundstrom, Full dispersion versus Debye model evaluation of lattice thermal conductivity with a Landauer approach, J. Appl. Phys. 109 (7) (2011): 073718
- [41] C. Jeong, S. Datta, M. Lundstrom, Thermal conductivity of bulk and thin-film silicon: a Landauer approach, J. Appl. Phys. 111 (9) (2012): 093708.
- [42] S. Datta, Electronic Transport in Mesoscopic Systems, Cambridge university press,
- [43] M. Lundstrom, Fundamentals of Carrier Transport, IOP Publishing, 2002.
- [44] J.R. Howell, M.P. Mengüç, K. Daun, R. Siegel, Thermal Radiation Heat Transfer, CRC press, 2020.
- [45] A. Majumdar, Microscale heat-conduction in dielectric thin-films, J. Heat Tran. 115 (1) (1993) 7–16.
- [46] F. Yang, C. Dames, Mean free path spectra as a tool to understand thermal conductivity in bulk and nanostructures, Phys. Rev. B 87 (3) (2013): 035437.
- [47] S. Lee, X. Li, Hydrodynamic phonon transport: past, present and prospects, in: Nanoscale Energy Transport: Emerging Phenomena, Methods and Applications, IOP Publishing, 2020.
- [48] M.F. Modest, Radiative Heat Transfer, second ed., Academic Press, Amsterdam; Boston, 2003.
- [49] D.Y. Li, Y.Y. Wu, P. Kim, L. Shi, P.D. Yang, A. Majumdar, Thermal conductivity of individual silicon nanowires, Appl. Phys. Lett. 83 (14) (2003) 2934–2936.
- [50] Q. Hao, Y. Xiao, Q. Chen, Determining phonon mean free path spectrum by ballistic phonon resistance within a nanoslot-patterned thin film, Mater Today Phys 10 (2019): 100126.
- [51] L. Yang, Y. Zhao, Q. Zhang, J.K. Yang, D.Y. Li, Thermal transport through fishbone silicon nanoribbons: unraveling the role of Sharvin resistance, Nanoscale 11 (17) (2019) 8196–8203.
- [52] J.K. Yu, S. Mitrovic, D. Tham, J. Varghese, J.R. Heath, Reduction of thermal conductivity in phononic nanomesh structures, Nat. Nanotechnol. 5 (10) (2010) 718–721.
- [53] J.Y. Tang, H.T. Wang, D.H. Lee, M. Fardy, Z.Y. Huo, T.P. Russell, P.D. Yang, Holey silicon as an efficient thermoelectric material, Nano Lett. 10 (10) (2010) 4279–4283.
- [54] L. Cui, S.Q. Shi, Z. Li, G.S. Wei, X.Z. Du, Reduction of thermal conductivity in silicene nanomesh: insights from coherent and incoherent phonon transport, Phys. Chem. Chem. Phys. 20 (42) (2018) 27169–27175.
- [55] Z. Xiong, X.Y. Wang, K.H.K. Lee, X.J. Zhan, Y. Chen, J.Y. Tang, Thermal transport in supported graphene nanomesh, ACS Appl. Mater. Interfaces 10 (11) (2018) 9211–9215.
- [56] W. Park, J. Sohn, G. Romano, T. Kodama, A. Sood, J.S. Katz, B.S. Kim, H. So, E. C. Ahn, M. Asheghi, Impact of thermally dead volume on phonon conduction along silicon nanoladders, Nanoscale 10 (23) (2018) 11117–11122.